

Data-Driven Surrogate Modeling Techniques to Predict the Effective Contact Area of Rough Surface Contact Problems

Tarik Sahin^{1*}, Jacopo Bonari², Sebastian Brandstaeter¹, Alexander Popp^{1,2}

¹Institute for Mathematics and Computer-Based Simulation (IMCS), University of the Bundeswehr Munich, Werner-Heisenberg-Weg 39, Neubiberg, D-85577, Bavaria, Germany.

²Institute for the Protection of Terrestrial Infrastructures, German Aerospace Center (DLR), Rathausallee 12, Sankt Augustin, D-53757, North Rhine-Westphalia, Germany.

*Corresponding author(s). E-mail(s): tarik.sahin@unibw.de;

Contributing authors: jacopo.bonari@dlr.de; sebastian.brandstaeter@unibw.de;
alexander.popp@unibw.de;

Abstract

The effective contact area in rough surface contact plays a critical role in multi-physics phenomena such as wear, sealing, and thermal or electrical conduction. Although accurate numerical methods, like the Boundary Element Method (BEM), are available to compute this quantity, their high computational cost limits their applicability in multi-query contexts, such as uncertainty quantification, parameter identification, and multi-scale algorithms, where many repeated evaluations are required. This study proposes a surrogate modeling framework for predicting the effective contact area using fast-to-evaluate data-driven techniques. Various machine learning algorithms are trained on a precomputed dataset, where the inputs are the imposed load and statistical roughness parameters, and the output is the corresponding effective contact area. All models undergo hyperparameter optimization to enable fair comparisons in terms of predictive accuracy and computational efficiency, evaluated using established quantitative metrics. Among the models, the Kernel Ridge Regressor demonstrates the best trade-off between accuracy and efficiency, achieving high predictive accuracy, low prediction time, and minimal training overhead-making it a strong candidate for general-purpose surrogate modeling. The Gaussian Process Regressor provides an attractive alternative when uncertainty quantification is required, although it incurs additional computational cost due to variance estimation. The generalization capability of the Kernel Ridge model is validated on an unseen simulation scenario, confirming its ability to transfer to new configurations. Database generation constitutes the dominant cost in the surrogate modeling process. Nevertheless, the approach proves practical and efficient for multi-query tasks, even when accounting for this initial expense. In summary, this work advances rough surface contact modeling into previously prohibitive application domains by integrating machine learning with efficient numerical simulation.

Keywords: Rough surface contact, Surrogate modeling, Machine learning, Boundary Element Method

1 Introduction

The vast majority of real surfaces, either natural or artificial, only collide within a small set of touching points or touching zones when brought into contact under moderate pressure. This defines a so-called effective contact area much smaller than the nominal contact area observed at a scale comparable to the surface extension in space. The reason for this behavior is that surfaces are affected by finely spaced irregularities and deviations from the ideal shape that include scratches, pits, grooves and, in general, jaggedness resulting from external factors or machining processes, with characteristic dimensions spanning several different scales. These imperfections are referred to, in the literature, as *surface roughness*, for which a comprehensive theory relevant to surface metrology can be found in Whitehouse [1].

The correct assessment of the effective contact area is a problem of paramount importance in numerous engineering and physics applications, since this quantity governs many coupled multi-physics phenomena happening at the contact interface, either mechanical, thermal or electrical. The excellent review presented in the work of Vakis et al. [2] accurately describes this complex scenario, referred to by the authors as a true “*paradise of multiphysics*”.

As a direct consequence of the utmost importance of this topic, a vast ecosystem of solution methods has developed over the last decades, which could be broadly categorized into analytical and numerical approaches. The first modern quantitative approach belongs to the first class and dates back to the seminal work of Greenwood and Williamson [3]. They developed the first multi-asperity model for the analysis of the relationship between real contact area and normal reaction force in a rough contact, and paved the way for all the subsequent analytical models whose detailed descriptions would, unfortunately, fall outside the scope of the presented publication. The interested reader is referred to Barber [4, §6] for a thorough list and detailed breakdown of the most important analytical models that have been developed during the last eighty years. These models have all proven to be excellent tools to gain a deep and fundamental understanding of the problem

under examination, and they are still used nowadays given their accuracy and speed of deployment. Nonetheless, they are characterized by some intrinsic limitations that make them unsuitable concerning various specific contexts. Analytical models are limited to derive results in a global sense, meaning that they can not deliver local information for specific points of the interface and, furthermore, have to rely on strong assumptions regarding surface geometry. To overcome their limitations, and thanks to the dramatic increase in terms of computational resources available, several numerical models have been developed parallel to analytical models for approximating solutions of rough contact problems. As of today, three main approaches, two based on continuum mechanics and one on atomistic models, are commonly used as computational workhorses for the numerical treatment of rough contact problems. Within the first category fall the Boundary Element Method (BEM), developed by Johnson [5] and specifically elaborated for rough contact by Xu and Jackson [6], and the Finite Element Method (FEM), for which related comprehensive computational contact schemes have been proposed by Wriggers [7], Popp et al. [8], Wriggers and Popp [9] for example with suitable numerical algorithms and solvers contributed by Adams [10], Wiesner et al. [11, 12] or Mayr and Popp [13].

In BEM models, the rough contact problem is cast as the equivalence between the interface displacement field and a Boundary Integral Equation (BIE) coincident with the spatial convolution over the contact domain between a Green’s function and an unknown contact traction field. In BEM, the problem complexity is reduced by one dimension, thus making it a very efficient tool, capable of delivering very accurate information on local displacements and contact tractions, see for example Pohrt and Li [14], Vollebregt [15], or Bemporad and Paggi [16] for a review of different possible implementations of the method. Since global quantities can be directly derived, it also proved itself a suitable tool for the comparison of the results delivered by different analytical models. Systematic research on this subject can be found in Paggi and Ciavarella [17], Carbone and Bottiglione [18], and Yastrebov et al. [19]. Despite this method being capable of analyzing any kind of surface without a priori assumptions on the asperities distribution, one drawback is that it is

mostly limited to infinitesimal strain and linear material laws. Extensions of the method can be found to account for bulk plasticity, viscoelasticity or generic conditions for which a Green’s function is not available in analytical form, see e.g. Jacq et al. [20], Putignano and Carbone [21], and Zhao et al. [22] for respective exemplary instances of these three cases. They unfortunately remain limited niche exceptions.

On the other hand, the FEM is much more versatile, since it can deal with the desired material law, finite deformations, finite size domains and complex boundary conditions. As a drawback, every part of the domain has to be discretized, so that the higher computational cost must be justified by specific requirements for the problem to be solved. The last twenty years have seen a continuous growth of the use of the FEM applied to the context under examination. In this regard, the first example can be traced back to Hyun et al. [23] for the adhesiveless frictionless contact between elastic bodies with rough surfaces, later extended by Pei et al. [24] to account for an elastoplastic response. The FEM has also been employed by Yastrebov et al. [25] for the solution of rough contact with finite plastic deformations and in Carvalho et al. [26] for the solution of Signorini problems involving deformable bodies in contact with geometrically complex rigid surfaces. Recently, a new method has been developed by Paggi and Reinoso [27] for a simplified yet accurate analysis of rough contact problems using FEM, in which the rough surface needs not to be explicitly modeled, but its shape is embedded in a layer of interface finite elements. The method, named *MPJR* (eMbedded Profile for Joint Roughness), was originally designed for the solution of two-dimensional adhesive rough contact problems, and has later been extended in Bonari et al. [28] to include friction and in Bonari et al. [29] to solve three-dimensional contact. The framework aims at bypassing some shortcomings that are faced when solving rough contact problems using FEM, namely the care required in the mesh generation process to avoid negative Jacobians and the difficulty related to the explicit discretization of the rough geometry.

Molecular Dynamics (MD) methods fall within the last category of numerical models. They can trace the kinematics of every single atom by computing its interaction with all particles in the

domain, using a predefined potential. Since every atom has to be explicitly modeled, the dynamic interaction time scales are inherently low, and the method is therefore particularly suitable for the analysis of very limited space and time domains; cf. [2, §2.5]. To overcome this, the elastic potentials of a single layer of atoms can be normalized to incorporate the elastic interactions proper to a semi-infinite solid. This Green’s Function Molecular Dynamics (GFMD) approach, developed by Campañá et al. [30], proved to deliver very accurate solutions, as demonstrated by the results of the recent contact mechanics challenge issued by Müser et al. [31].

To leverage the advantages of one method over its drawbacks, multi-scale approaches can be defined, in which different models are employed for the solution of different scales of the problem, with information exchange enforced across the scales. In Bonari et al. [32], FEM is used at the macro-scale, where a perfectly smooth interface is considered, while BEM is employed for the solution of a micro-scale rough contact problem. A bidirectional coupling between the two scales is enforced in terms of mean-plane separation.

Despite the huge steps forward in numerical solution schemes, and even though the available computational resources continuously increased, the high-fidelity numerical solution of a rough contact problem can still be cumbersome. An excellent example are parameter studies, where numerous simulations have to be run, causing the computational cost to grow rapidly and eventually become prohibitive. For instance, in the context of optimizing material properties or surface topographies for improved contact performance, multiple simulations are required to evaluate different design parameters, making high-fidelity modeling computationally expensive.

In this regard, a possible solution is offered by the huge advancement and development experienced in the last few years by efficient surrogate modeling techniques. Among them a promising approach, namely data-driven surrogate modeling, is based on experimental or synthetically generated data, thus deliberately excluding a physics-based modeling of the system; instead, the model extracts underlying patterns in provided data by deploying machine learning algorithms. Many application cases of data-driven surrogate modeling techniques specifically crafted for the realms of

science and engineering are available in the literature [33–36]. These techniques aim to achieve high accuracy while requiring minimal computational or prediction time.

Data-driven surrogate modeling techniques can be developed for various purposes such as prediction, parameter identification, classification, and anomaly detection. When focusing on rough surfaces, these techniques find application across a diverse range of scenarios in fluid mechanics, tribology, and contact mechanics. Sanhueza et al. [37] deployed machine learning as a parameter identifier to predict the behavior of turbulent flows past rough surfaces. They applied convolutional neural networks on the height map of a rough surface to identify the corresponding skin friction values and Nusselt numbers. Elangovan et al. [38] employed multiple linear regression to identify surface roughness in turning operations by considering machining parameters such as speed, depth of cut and tool wear. The resulting database comprises statistical features derived from vibration signals, and, in addition, principal component analysis is applied to reduce the dimensionality of the input space. In the study by Prajapati et al. [39] the researchers constructed a surrogate model utilizing a regression-based Multi-Layer Perceptron (MLP) to predict elastohydrodynamic lubrication parameters, specifically the traction coefficient and asperity load ratio. These predictions were customized for different surface topographies encountered in rough contact problems. Similarly, Boidi et al. [40] applied the machine learning radial basis function method to identify the coefficient of friction on textured and porous surfaces. In addressing rough surface problems, there are numerous additional examples where machine learning techniques have been applied to identify parameters associated with surface roughness, lubrication and wear. This is well-documented in the reviews by Syam [41] and Batu [42]. However, only a few studies have delved into predicting the mechanical response associated with contact problems on rough surfaces, such as the prediction of effective contact area and contact force. In the work led by Rapetto et al. [43], the authors explored the ability of neural networks to predict the relation between roughness parameters and the effective contact area. The generated dataset comprises statistical features derived solely from 2D profiles, with

the authors noting that the error tends to be higher for small values of the effective contact area. Similarly, Kalliorinne et al. [44] explored the ability of multitask neural networks to predict the mechanical response of contact, including the effective contact area and contact pressure, across surface topographies generated using distinct methods based on a given heights probability distribution and power spectrum. In research conducted by Jiang et al. [45], a new method was proposed to predict the effective contact area of fractal rough surfaces. This method employs a regression model based on least-squares support vector machines. As the fractal surfaces are generated using a deterministic Weierstrass-Mandelbrot (WM) model, the resulting database does not include the statistical features but comprises solely the roughness parameters inherent to the WM model and the external load. Furthermore, the generated database has a very limited range due to costly FEM simulations. Additionally, they do not report generalization errors on the unseen data since only a single sample is left for testing. Another approach for generating a surrogate model, namely Physics-Informed Neural Networks (PINNs), incorporates the physical laws of a governing problem and the additional data into the loss function of the neural networks [46]. For instance, in the context of contact mechanics, Sahin et al. [47] deployed PINNs as a fast-to-evaluate surrogate model to solve forward and inverse contact mechanics problems on the macro-scale.

As stated above, only very few studies have focused on predicting the effective contact area in contact problems involving rough surfaces, employing state-of-the-art data-driven techniques. Therefore, there is a continuous demand for the development of such techniques. In this manuscript, we develop a surrogate modeling framework to predict the effective contact area stemming from the contact between a linear elastic half-space and a rigid rough surface. Rough topographies are generated utilizing the RMD algorithm to obtain self-affine fractal surfaces. The generated database includes a wide range of parameters, viz. model parameters, material parameters and roughness parameters obtained through statistical characterization of topographies. These statistical roughness parameters are calculated based on the height field, summits

(maxima in 3D) and peaks (maxima in 2D) of fractal surfaces. In contrast to earlier investigations in the literature, various machine learning algorithms are deployed as fast-to-evaluate models utilizing a database generated with Boundary Element Method simulations. As mentioned earlier, BEM stands out as an efficient approach, providing highly accurate results with significantly reduced computational time compared to other numerical schemes. Thus, we couple state-of-the-art data-driven methodologies with enriched simulation data based on BEM. These methodologies include Decision Tree, Random Forest, Support Vector Machine (SVM) Regressor, Adaptive Boosting (AdaBoost), Gaussian Process (GP) Regressor, Gradient Boost, Kernel Ridge, eXtreme Gradient Boosting (XGBoost), and Multi-Layer Perceptron (MLP) Regressor. Hyperparameter optimization is performed to identify the best configuration for each model type. This optimization is carried out through grid search combined with cross-validation to identify the optimal model parameters. For quantitative comparisons among surrogate models, several accuracy metrics are computed. These metrics include the normalized mean square error (nMSE), normalized mean absolute error (nMAE), normalized max-error (nMaxE) and the R^2 score. Selecting an optimal surrogate model requires balancing accuracy and prediction performance, depending on the specific requirements of the application task. Our results indicate that kernel-based regressors generally perform very well in the given context of rough surface contact simulations. Among them, the Kernel Ridge model offers the best trade-off between accuracy and computational efficiency. It achieves high predictive accuracy, low prediction time, and minimal training overhead, making it a strong candidate for general-purpose surrogate modeling. Therefore, the Kernel Ridge model is eventually compared to the BEM model in terms of overall computational time. This assessment encompasses not only the prediction time of the trained model but also considers the training, tuning, and data generation time. Going one step further, to assess the model’s generalization capability, the optimal model is tested in a new simulation scenario, which is not seen during the training process. The findings reveal that the developed surrogate model performs well in this previously unseen scenario. Specific scientific

contributions of the paper can be outlined as follows:

- Development of an efficient fast-to-evaluate surrogate modeling workflow to predict the effective contact area for rough surface contact problems.
- Establishment of an informative database encompassing a diverse set of parameters combined with BEM simulations.
- Generalization of the machine learning model by testing on the unseen simulation scenario.

The remainder of this article is structured as follows. Section 2 describes the problem formulation of rough surface contact between a linear elastic half-space and a rigid rough surface generated by the Random Midpoint Displacement (RMD) algorithm. An efficient numerical approach, the BEM, is outlined as a state-of-the-art method to compute the effective contact area. Also, a variety of statistical parameters are used to describe surface features, thus creating a meaningful database for surrogate modeling. In Section 3, we elucidate a methodology for surrogate modeling as an alternative to conventional techniques. This includes the development of a surrogate modeling workflow, the generation of a database exploiting BEM simulations, and the introduction of fast-to-evaluate surrogate models as baseline models and tuned models via hyperparameter optimization. Furthermore, several accuracy metrics are introduced to validate the accuracy of surrogate models. Section 4 covers an evaluation of baseline and tuned models comparing them in terms of accuracy and performance. Among the investigated machine learning approaches, the so-called optimal model is compared with the BEM model in terms of performance. Also, the optimal model (Kernel Ridge) is evaluated in a different environment with unseen data. Section 5 concludes the manuscript by summarizing the main findings and providing insights into future research directions.

2 Problem Formulation

2.1 Physical Problem: Rough Surface Contact

A rough surface contact problem typically refers to a class of engineering challenges that involves the

interaction between two surfaces which are conformal at the macro-scale, but non-conformal at smaller scales, given the presence of micro-scale textures, defects, or, in general, asperities [48].

The study of these problems stemmed from the attempt to explain Coulomb’s law of friction - specifically, the observation that the tangential force Q required for the relative sliding of two bodies in contact is proportional to the normal force P that pushes them together, and independent of the observable contact area [49]. However, at the microscopic level, real surfaces are rough and contact occurs only at discrete asperities, forming the effective contact area \mathcal{A}_e which is typically much smaller than the nominal contact area. This effective contact area plays a crucial role in friction, wear, and sealing mechanisms, as it governs the actual load-bearing capacity and energy dissipation at the interface [50]. Therefore, its correct assessment is essential for the analysis of physical phenomena related to friction, wear, and sealing, i.e., the class of problems investigated in the field of tribology [50]. On top of that, thanks to electro- and thermo-mechanical analogies [51], the effective contact area also plays a crucial role in the study of electrical and thermal exchanges at the interface level.

Many analytical models have been developed for the identification of the effective contact area in this context, but they rely on strong assumptions for the statistical distribution of the elevation field describing the rough surface and, most importantly, they deliver a global response that can not describe the solution at every point of the contact domain. In contrast, numerical models can not only estimate the effective contact area but also determine the contact status of each interface point—that is, identify which points are in contact and which are not.

A common numerical analysis approach is based on the hypothesis of scale separation. Consider the two bodies B_i , $i \in \{1, 2\}$, represented in Figure 1, brought into contact by the action of an external load, which can be an applied force or an imposed act of motion Δ , the latter going under the name of *far-field displacement*. We assume that the shapes of the contacting surfaces \mathcal{S}_i , which correspond to portions of the boundaries ∂B_i of the bodies, match or conform to each other, enabling the creation of a finite nominal

contact area. In this case, a nominally smooth contact interface Γ can be defined, encompassing \mathcal{S}_i along with the underlying portions of the material bulk.

We now assume that the contacting surfaces are microscopically rough, and focus the attention on a subset of Γ small enough to make the roughness characteristics relevant. This subset is referred to as a Representative Surface Element (RSE). In most cases analyzed in the literature, the RSE is modelled as a square patch with size L , discretized on a Cartesian grid with n points per side and grid size $g_l = L/(n - 1)$. On this grid, roughness is described by two discrete height fields $z_i \in \mathbb{R}^{n \times n}$, i.e., a height value for both rough surfaces is assigned to every node of the grid, calculated from a reference datum plane Ω for each of the surfaces \mathcal{S}_i .

If the macroscopic, nominally smooth contact interface Γ is flat, Ω can be considered as part of \mathcal{S}_i . Otherwise, it can be regarded as the tangent plane at the point under consideration: given the hypothesis of scale separation, we assume that the local radius of curvature R satisfies $R \gg L$, where R is the common local radius of curvature for both \mathcal{S}_i .

If this approach is chosen, a variable for the number of points in contact, n_c , can be introduced and the effective contact area for the RSE expressed as:

$$\mathcal{A}_e = 100 \frac{n_c g_l^2}{L^2} \%, \quad (1)$$

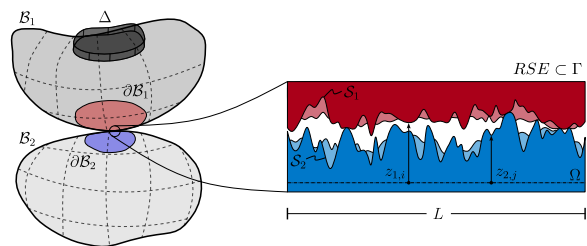


Fig. 1: Graphical representation of the problem under consideration. At a macroscopic scale, two deformable bodies come into contact under the action of an external imposed displacement Δ . At the microscopic scale, roughness features can be revealed, resulting in an effective contact area \mathcal{A}_e much smaller than the nominal contact area that is assumed at the macroscopic scale.

If the bodies in contact are linear elastic, the solution of the contact problem in terms of \mathcal{A}_e , or, equivalently, n_c , is only governed by the relative normal displacements \mathbf{u}_i of opposite points belonging to the two sides of Γ [51, §2.2]. Thanks to this property, the problem can be simplified and re-formulated as a contact problem involving a rough rigid surface characterized by a *combined height field* $\mathbf{z} = \mathbf{z}(\mathbf{z}_i) \in \mathbb{R}^{n \times n}$ and a semi-indefinite linear elastic half-space with *composite mechanical parameters* $E = E(E_i)$ and $\nu = \nu(\nu_i)$ cf. Figure 2. However, given the assumptions of linearity, and since for small values of \mathcal{A}_e a well acknowledged result in tribology is the proportionality between contact area and imposed load, it can be concluded that the actual pattern of contact spots is dictated by the surfaces topography only, and not by the value of the composite Young’s modulus.

In summary, the key parameters governing the computation of the effective contact area \mathcal{A}_e are the imposed load Δ and the surface height field \mathbf{z} . Thus, in abstract terms, solving the problem means evaluating the following function:

$$\mathcal{A}_e = f(\Delta, \mathbf{z}). \quad (2)$$

This problem setup is illustrated in Figure 3a. We know that such a functional relationship exists [], and that approximate well-known general closed-form expressions for f are available from many different classical analytical models. However, a lack of overall general agreement in terms of outcome is experienced, with different theories leading to slightly but non-negligible differences in their findings [52]. Furthermore, the derivation of closed form expressions comes with the cost of strong starting assumptions, e.g., in terms of the topography that must be considered. Instead, evaluating the function f without a priori simplifications requires the numerical solution of a boundary integral equation that models the whole contact mechanics problem. As described in Section 1, various numerical schemes can be employed to solve this problem. In this work, we use the Boundary Element Method (BEM) for which further details will be provided in Section 2.4.

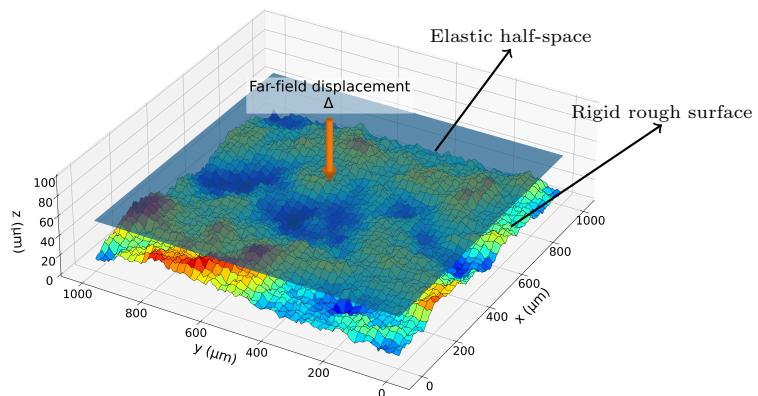


Fig. 2: Schematic depicting the standard rough surface contact problem. Since a composite formulation is applied, the rough surface is assumed to be rigid while the flat surface is linear elastic with composite material properties.

2.2 Random Midpoint Displacement Algorithm

In this study, we are interested in predicting the effective contact area for a given rough surface, encoded by its height profile \mathbf{z} . We use the Random Midpoint Displacement (RMD) algorithm to generate synthetic rough surfaces. RMD is a well-established method for producing surfaces with realistic properties. Originally introduced by Fournier et al. [53], it is commonly used to generate self-affine fractal surfaces [54]. This algorithm is a recursive process that starts from the known heights of four points located at the corners of a square grid made of a single cell with lateral side L . The cell is then split in four, resulting in a grid with nine nodes and four smaller cells with side $L/2$. Then, a height is assigned to each of the five newly created nodes. The height of the four nodes on the edges is given by the mean value of the heights of the two adjacent corner nodes plus a random perturbation extracted from a Gaussian distribution with zero mean and standard deviation σ_0 . The height of the central node is given by the mean value of the four corner nodes plus a random perturbation extracted from the same Gaussian distribution $\mathcal{N}(0, \sigma_0)$ used for the edge nodes. The process is repeated as many times as

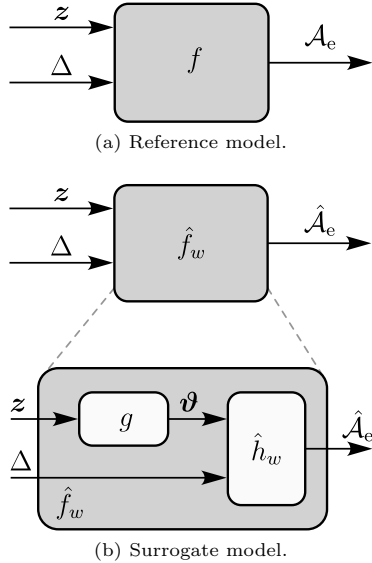


Fig. 3: Surrogate modeling framework for the effective contact area in rough surface contact: (a) the reference model f computes \mathcal{A}_e as a function of far-field displacement Δ and surface height field \mathbf{z} , requiring costly numerical simulations; (b) the surrogate model \hat{f}_w approximates this using a fast-to-evaluate regression model $\hat{h}_w(\Delta, \boldsymbol{\vartheta})$, where $\boldsymbol{\vartheta} = g(\mathbf{z})$ is a vector of statistical parameters. The function g is a known deterministic mapping that enables dimensionality reduction of the input vector.

desired, and for every iteration the standard deviation associated with the Gaussian distribution is scaled by a factor 2^{-H} , where H is the generalized Hurst exponent. In this study, a range between 0.5 and 0.8 is chosen for H . This range includes typical values observed in many artificial surfaces [54] and in various natural phenomena that exhibit fractal self-affinity [55–57]. The key point of the algorithm is the scaling law of the standard deviation: it can be proven that for this value the height variation between grid points separated by a distance $1/2^n$ is proportional to $1/2^{nH}$, as required by the definition of self-affine processes [56]. An illustrative example of how the RMD algorithm works is given in Figure 4. In the current study, surfaces with both 128×128 and 256×256 elements per side have been investigated, thus employing seven and eight iterations of the RMD algorithm, respectively.

2.3 Statistical Characterization of Topographies

Statistical characterization of rough surfaces plays an important role in identifying hidden patterns [58]. This result has been achieved by applying the Random Process Theory (RPT), previously employed in the study of random noise signals, to the surfaces under examination. Functional relationships can be drawn between the statistical parameters of the surfaces and the features of the related contact problem. As an example, many analytical models predict that the ratio between effective contact area and applied load is proportional to the mean square profile slope, which quantifies the average steepness of the surface asperities and is mathematically defined as the expectation of the squared derivative of the surface profile [59]. Furthermore, many legacy asperity-based normal contact models, most of them stemming from the pioneering works of Greenwood and Williamson [3], hinge on the distribution of the surface heights.

The statistical characterization can be performed by considering the surface as a 3D entity, sampling the height field and the summits (maxima in 3D) distributions, or by considering the surface as a global assembly of multiple 2D section

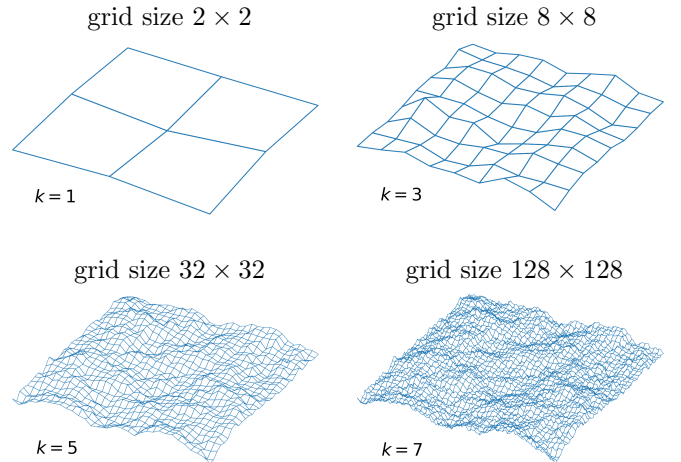


Fig. 4: An illustration of the *Random Midpoint Displacement* (RMD) algorithm. A higher interaction count k results in a finer discretization of the generated self-affine fractal surface.

cuts, or profiles, and then analyzing each profile's heights, slopes and peaks (maxima in 2D) distribution [60]. Peaks are measured on profiles generated by a profilometer which moves in both the x- and y-direction through the scan length of the topography as depicted in Figure 5a. A profile can be characterized by peak heights z_p , the maximum of peaks z_p^{\max} and the mean of peaks \bar{z}_p , see Figure 5b).

In the current work, the statistical parameters usually employed in classical mechanical models will be derived from the rough surfaces generated according to the procedure presented in Section 2.2 and used as input features for the purely data-driven model as presented in Section 3.1. Every quantity derived for this purpose is presented and listed in Table 1, which comprehensively lists all the statistical parameters used in this study.

2.4 State of the Art: BEM-based Numerical Simulations

As stated in Section 2.1, the solution of the rough contact problem requires the determination of surface displacements. The Boundary Element Method applied to rough contact problems [6] is a robust numerical workflow to obtain boundary displacements u at the frontier of a deformable body, in this case a linear elastic half-space. The formulation of the continuous problem starts from the closed-form convolution of an applied traction field p with a Green's function that can be expressed as the following Boundary Integral Equation (BIE):

$$u(x, y) = \frac{1 - \nu^2}{\pi E} \int_{\mathcal{S}} \frac{p(\xi, \eta)}{\sqrt{(x - \xi)^2 + (y - \eta)^2}} d\xi d\eta. \quad (3)$$

Assuming the action of the vertical far-field displacement Δ , that pushes the bodies in contact, an indentation level \bar{u} can be defined that quantifies the interference of the rough surface and the half-space, see Figure 6. The introduction of this quantity allows to state the contact problem as an infinite dimensional Linear Complementarity Problem (LCP):

$$\begin{aligned} w(x, y) &\geq 0, & p(x, y) &\geq 0, \\ w(x, y)p(x, y) &= 0, \end{aligned} \quad (4)$$

where $w = u - \bar{u}$. Equations (3) and (4) above can be discretized on the Cartesian grid introduced in Section 2.1, resulting in the finite dimensional LCP:

$$\begin{aligned} \mathbf{w} &\geq 0, & \mathbf{p} &\geq 0, \\ \mathbf{w} \cdot \mathbf{p} &= 0, & \mathbf{u} &= \mathbf{H} \cdot \mathbf{p}, \end{aligned}$$

where the discretized field variables $\mathbf{w} \in \mathbb{R}^{n \times n}$ and $\mathbf{p} \in \mathbb{R}^{n \times n}$ are coincident with the integral average value of the equivalent continuous quantities, evaluated in correspondence of the center of each cell g_c . Under linear elasticity assumptions it can be proven that \mathbf{H} is symmetric and positive definite and that the problem has a unique solution. The values to be used in the definition of the matrix \mathbf{H} are dependent on the discretization framework employed. The interested reader is pointed to, among the others, for possible choices of the influence coefficients [14, 16].

Several open-source codes are available to solve rough contact problems using the formulation presented above, e.g. *MIRCO* (co-developed by the authors themselves) [57], *Tamaas* [61], and *MultiFEBE* [62]. Since we aim at simulating linear elastic frictionless contact between a rigid rough indenter and an elastic half-space, *MIRCO* is used to run the numerical simulations. Figure 7 presents example results from contact simulations using two different surface topographies created by the RMD, and two indentation levels, $\Delta_0 = 25 \mu\text{m}$ and $\Delta_1 = 35 \mu\text{m}$. For the same topographies, given in Figure 7a and Figure 7b, increasing the indentation level leads to a larger effective contact area, as shown in Figure 7d and Figure 7e. On the other hand, for the same indentation level (see Figures 7a and 7c), two different topographies can lead to very different effective contact areas. The surface in Figure 7c is much smoother and consequently more points get in contact as can be seen from the resulting contact force distributions in Figures 7d and 7f.

Furthermore, to illustrate the accuracy of *MIRCO*, a benchmark example, namely the contact problem between an elastic half-space and a smooth paraboloid rigid indenter [63], is investigated. Analytical solutions for the contact force F and the normalized contact area A_n can be obtained as:

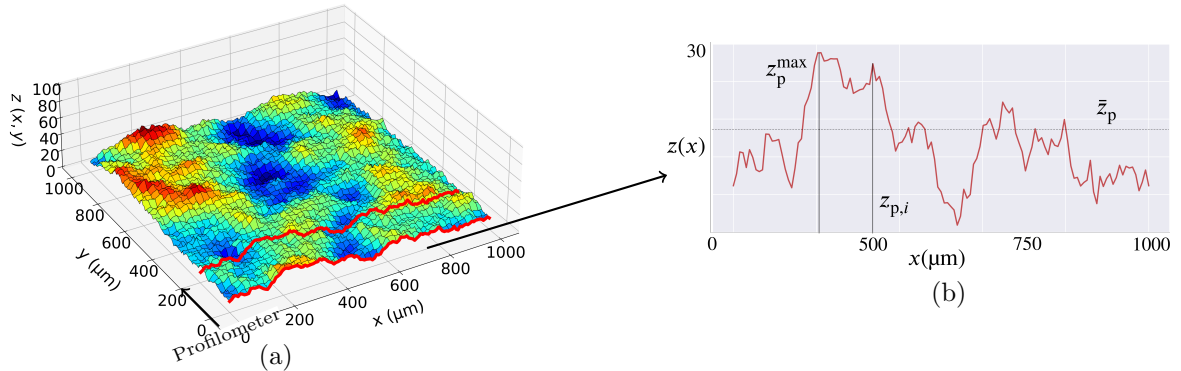


Fig. 5: (a) 3D representation of a rough topography. (b) A corresponding 2D profile characterized by specific statistical parameters, such as peak heights $z_{p,i}$ with accompanying maximum and mean values, z_p^{\max} , \bar{z}_p , respectively.

$$F = \frac{4}{3} \frac{E}{1-\nu^2} \sqrt{R\Delta^3} \quad \text{and} \quad A_n = 100 \frac{\pi R \Delta}{L^2}, \quad (5)$$

where R is the minimum radius of curvature of the paraboloid. For our specific setup, we set $R = 5,000 \mu\text{m}$, $L = 1,000 \mu\text{m}$, and Δ linearly varying from $0 \mu\text{m}$ to $1 \mu\text{m}$. Figure 8 shows a comparison between the analytical solution and two numerical solutions obtained using BEM with two different grid discretizations of 128×128 and 256×256 points per side. As shown in Figure 8a, the contact force computed using BEM matches the analytical solution well for both grid resolutions. In contrast, the computed contact area slightly underestimates the analytical solution at higher resolution, and is even smaller with the coarser grid, as illustrated in Figure 8b. These deviations stem from the method

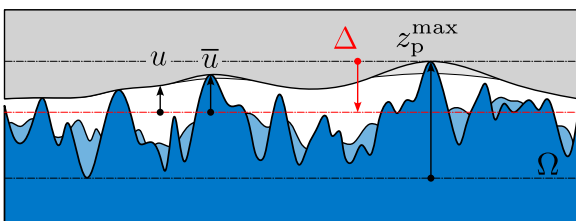


Fig. 6: Under the action of the vertical far-field displacement Δ , the deformable bodies are pushed into contact. To properly formulate the LCP problem, an interference \bar{u} can be defined, equal, at each node, to $z - (z_p^{\max} - \Delta)$.

used to calculate the effective contact area. A simple method is used to estimate the contact area by dividing the number of contact nodes by the total number of nodes on the micro-scale surface. As a result, the finer grid leads to lower errors and smoother results.

Although BEM is an efficient method, simulations can still become computationally expensive. Figure 9a presents the simulation times for different combinations of far-field displacements and surface realizations. Each point represents the simulation time for a randomly generated surface and a specific value of the far-field displacement. All surfaces are discretized on a 128×128 grid. The simulation time varies significantly across different far-field displacements. Additionally, there is considerable variability in simulation time even for the same far-field displacement, which can be attributed to differences in surface properties. Generally, larger far-field displacements and smoother surfaces result in longer simulation times. Notably, both higher far-field displacements and smoother surfaces are associated with increased contact areas. Figure 9b illustrates this trend by showing the relationship between simulation time and effective contact area. Clearly, larger contact areas lead to longer simulation times.

The simulation time for a single run can reach up to approximately 1,750 s. While relatively low compared to other large-scale models,

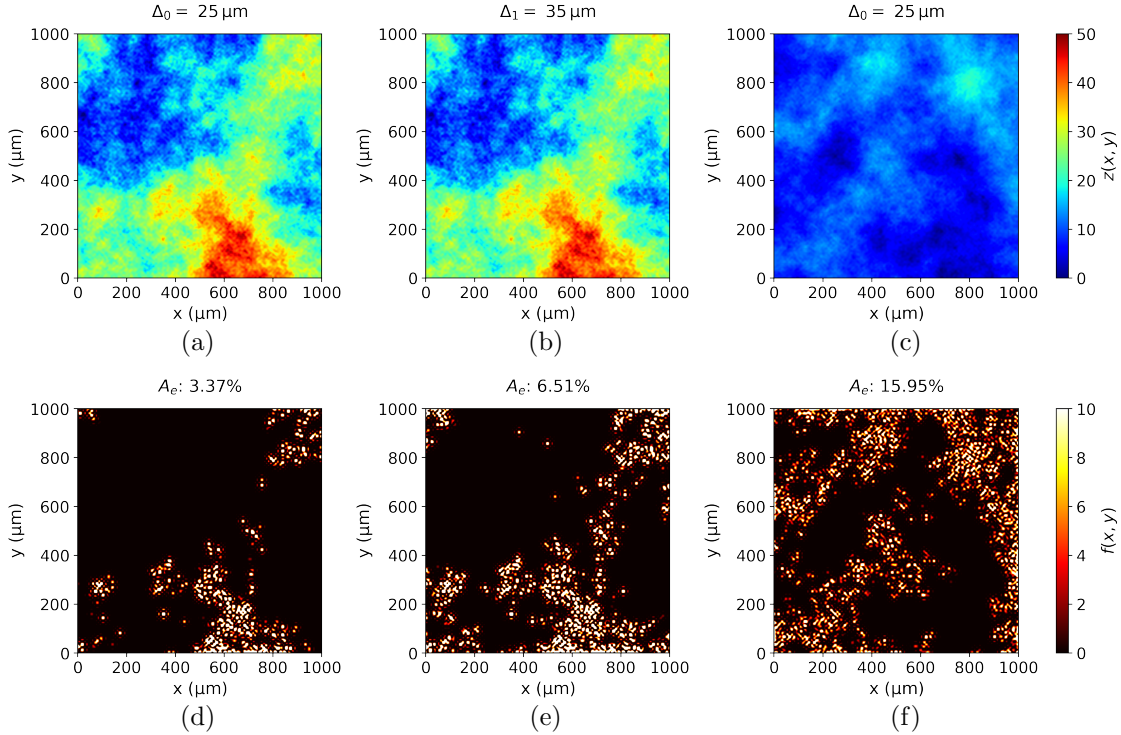


Fig. 7: The top row of images (Fig. a-c) shows two surface topographies generated by the RMD. Dark blue indicates the deepest valleys, while dark red represents the highest summits. The bottom row of images (Fig. d-f) shows the resulting contact force per grid point f , for two far-field displacements $\Delta_0 = 25 \mu\text{m}$ and $\Delta_1 = 35 \mu\text{m}$. The corresponding effective contact area \mathcal{A}_e is also shown.

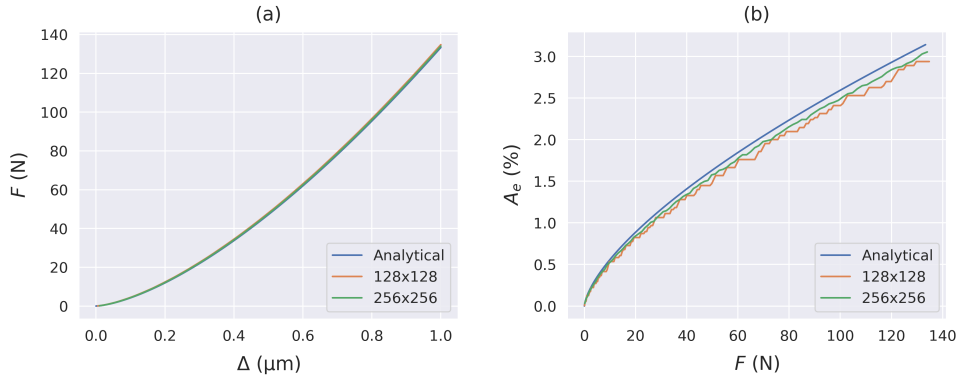


Fig. 8: Comparison between analytical and BEM solutions for the paraboloid rigid indenter example. BEM models have surfaces discretized on a grid with 128×128 and 256×256 points per side, respectively.

this still makes multi-query analyses computationally expensive. Such analyses—including parameter studies, sensitivity analysis, uncertainty quantification, and parameter identification—are crucial for many real-world applications. For example, parameter studies and sensitivity analysis

explore the influence of variables like grid size or far-field displacement, while uncertainty quantification evaluates how input uncertainties affect model outputs. [64, 65] Parameter identification, on the other hand, aims to infer model parameters

from data. [66, 67] All these tasks require running the model many times—often several thousands—making them potentially prohibitively expensive due to the computational cost of individual BEM simulations. Similarly, multi-scale algorithms—where different models are used to resolve different scales of a problem, with information exchanged between scales—can become prohibitively expensive even for moderately sized problems due to their nested simulation structure. For instance, a micro-scale BEM simulation may be required at each Gauss point of a continuum FEM simulation. [32] To alleviate this computational burden, data-driven surrogate models can be employed to replace the costly micro-scale simulations, thereby making large-scale multi-scale analyses significantly more tractable and computationally efficient.

2.5 Data-driven problem: learning a surrogate model

Surrogate modeling aims to reduce computational costs by approximating complex, computationally expensive models with more efficient alternatives. Often, this reduction in computational cost comes at the expense of model accuracy and generality. Surrogate models can take various forms, such as analytical models [68], physics-informed machine learning models [69], or purely data-driven approaches based on machine learning techniques [70]. The choice of surrogate model depends on the desired balance between model accuracy, generality, and computational efficiency.

Mathematically, the data-driven surrogate modeling task can be formulated as a regression task. Given a dataset (or database) $\mathcal{D} = \{(\mathbf{x}_i, y_i)\}_{i=1, \dots, N}$ of N pairs of inputs \mathbf{x}_i and corresponding outputs $y_i = f(\mathbf{x}_i)$, the goal is to learn a function $\hat{f}_{\mathbf{w}} : \mathbb{R}^d \rightarrow \mathbb{R}; \mathbf{x} \mapsto \hat{y} = \hat{f}_{\mathbf{w}}(\mathbf{x})$ that approximates the true model $f : \mathbb{R}^d \rightarrow \mathbb{R}; \mathbf{x} \mapsto y = f(\mathbf{x})$ such that

$$\hat{f}_{\mathbf{w}} \approx f, \quad (6)$$

where $\mathbf{x} \in \mathbb{R}^d$ is the d -dimensional vector of input parameters, $y \in \mathbb{R}$ is the scalar quantity of interest (or target quantity), $\hat{y} \in \mathbb{R}$ is the approximation of the quantity of interest by the surrogate model, and \mathbf{w} are the free parameters of the surrogate

model. Learning the surrogate model $\hat{f}_{\mathbf{w}}$ typically involves minimizing a loss function

$$\mathcal{L}(\mathcal{D}, \hat{f}_{\mathbf{w}}) = \sum_{i=1}^N (y_i - \hat{y}_i)^2, \quad (7)$$

with respect to the free parameters \mathbf{w} , where $\hat{y}_i = \hat{f}_{\mathbf{w}}(\mathbf{x}_i)$ denotes the surrogate prediction at sample point \mathbf{x}_i .

Given this mathematical framework, we propose a data-driven surrogate modeling workflow to reduce the cost of evaluating the effective contact area in rough surface contact problems, which depend on the far-field displacement Δ and the surface height field \mathbf{z} , as defined in Section 2.1. In this context, the system is described by the function f introduced in Equation (2) and illustrated in Figure 3a. The input vector is defined as $\mathbf{x} = [\Delta, \mathbf{z}]$, and the target quantity is $y = \mathcal{A}_e$. We aim to approximate f using a surrogate model $\hat{f}_{\mathbf{w}}$, as depicted in Figure 3b.

A central challenge in this problem is the high dimensionality d of the input vector, primarily due to the discretized height field \mathbf{z} . To address this, we adopt a dimensionality reduction approach: instead of using \mathbf{z} directly, we represent it through a set of summary statistics or statistical descriptors $\boldsymbol{\vartheta}$ (cf. Section 2.3). This significantly reduces the input dimensionality, as $\boldsymbol{\vartheta}$ captures the essential characteristics of \mathbf{z} with far fewer parameters.

Moreover, while the dimensionality of \mathbf{z} increases with the grid size (e.g., 1024 for a 32×32 grid and 16384 for a 128×128 grid), the number of statistical parameters in $\boldsymbol{\vartheta}$ remains fixed. In this study, we compute 22 such statistical parameters, enabling efficient and scalable surrogate modeling.

Ultimately, the surrogate model $\hat{f}_{\mathbf{w}}$ can be equivalently described by the following set of equations:

$$\hat{\mathcal{A}}_e = \hat{f}_{\mathbf{w}}(\Delta, \mathbf{z}) \iff \begin{cases} \boldsymbol{\vartheta} & = g(\mathbf{z}), \\ \hat{\mathcal{A}}_e & = \hat{h}_{\mathbf{w}}(\Delta, \boldsymbol{\vartheta}), \end{cases} \quad (8)$$

Here, g is a known deterministic function that maps the height field \mathbf{z} to a vector of statistical descriptors $\boldsymbol{\vartheta}$ (as detailed in Section 2.3), and $\hat{h}_{\mathbf{w}}$ is a regression model trained from data. This model is learned using the dataset $\mathcal{D} = \{([\Delta_i, \boldsymbol{\vartheta}_i], \mathcal{A}_e^i)\}_{i=1, \dots, N}$, where each $\boldsymbol{\vartheta}_i = g(\mathbf{z}_i)$.

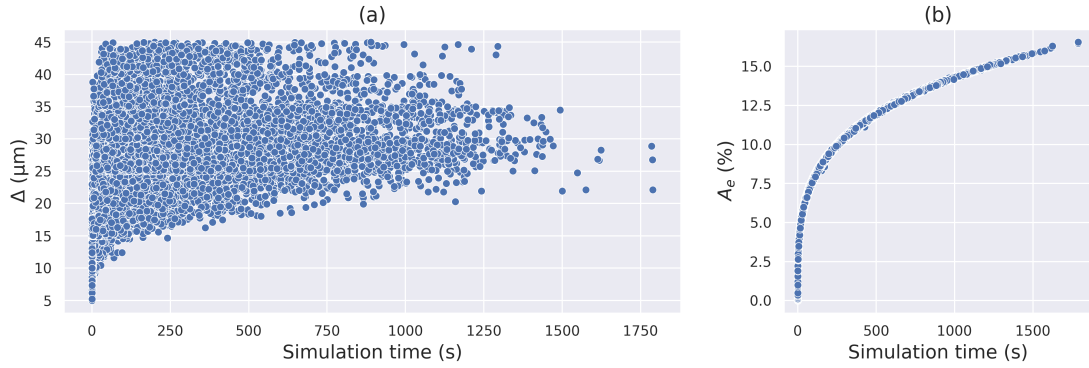


Fig. 9: Comparison of simulation time for rough surface contact simulations with a grid size of 128×128 . (a) shows the effect of different far-field displacements and surface realisations on the overall simulation time. Each point represents a randomly generated surface and a specific far-field displacement. (b) The correlation between effective contact area and simulation time.

A graphical representation of Equation (8) is shown in Figure 3b. Once the model \hat{h}_w is trained, evaluating the surrogate on a new, unseen rough surface involves computing its statistical descriptors via g and applying the learned regression model as outlined in Equation (8). While the original model f could also be used to predict the target quantity, doing so would incur significant computational cost. In contrast, evaluating the surrogate model is substantially faster, making it particularly well-suited for multi-query analysis scenarios (cf. previous section), where thousands of such model evaluations may be required.

3 Methodology

3.1 Surrogate Modeling Workflow

After mathematically defining the problem setup in the previous section, we describe the full modeling workflow from a practical perspective. The proposed modeling workflow is illustrated in Figure 10. First, we define the input parameter space and sample from it. The input parameter space consists of the statistical parameters of a rough surface and the far-field displacement. We use controlled sampling [71] to explore this space. While the far-field displacement can be sampled directly, the surface parameters are sampled indirectly: a random rough surface is first generated using the RMD algorithm (see Section 2.2), and its statistical parameters are then computed as described in Section 2.3.

Second, we run BEM simulations for all input samples (pairs of rough surfaces and far-field displacements) to compute the corresponding effective contact areas. In this way, we construct a database \mathcal{D} consisting of input-output samples. An important practical aspect of data-driven surrogate modeling is data preprocessing, which follows database generation. Not all parameters may be relevant, and some data points might be incomplete, e.g., due to failed BEM simulations. Thus, methods such as feature selection and data cleaning are applied to obtain the final form of the database [72]. Feature selection is the process of identifying and selecting a subset of the most relevant input parameters (features) from the dataset that contribute the most to the model’s predictive performance. The goal is to improve model accuracy, reduce overfitting, and decrease training time by removing irrelevant, redundant, or noisy features. Data cleaning is used to remove missing values resulting from failed simulations. Moreover, data normalization [72, 73] is applied to scale the problem and improve model performance and stability.

Third, various machine learning regression models are trained as fast-to-evaluate surrogate models, and hyperparameter optimization is performed to tune them further. Due to the *black-box* nature of purely data-driven methods, human oversight is necessary throughout the training process. This includes defining the hyperparameter search space, managing the workflow, making critical decisions, and selecting the optimal model.

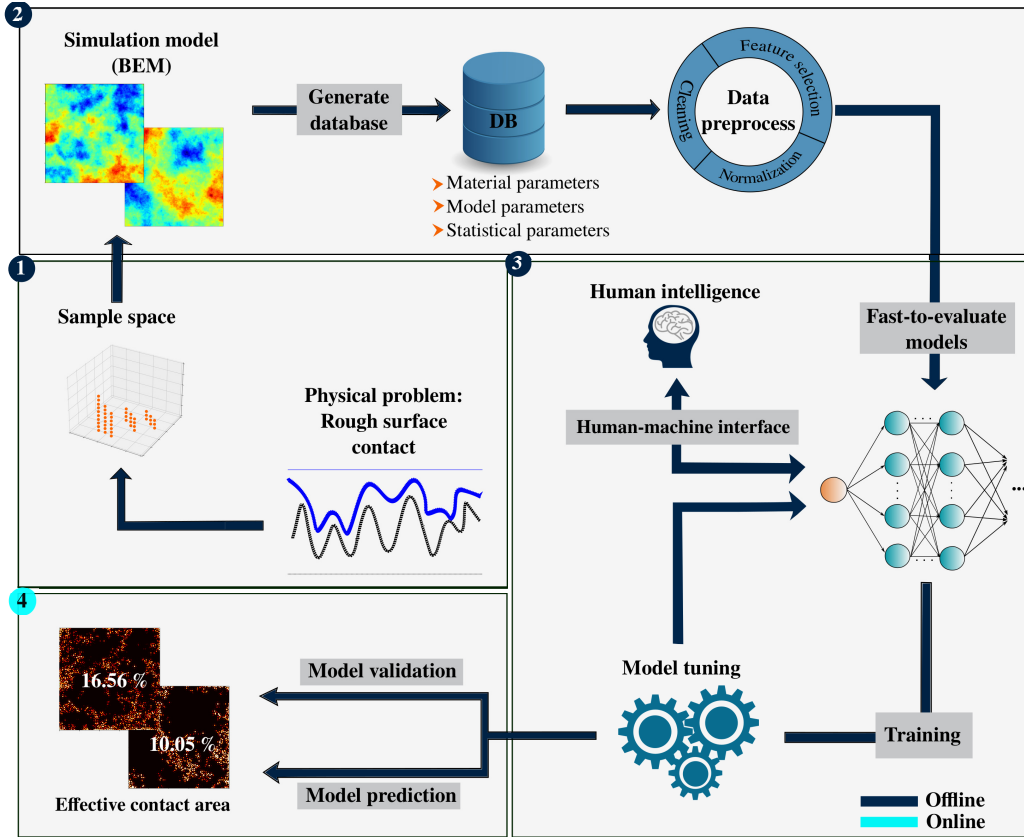


Fig. 10: Data-driven surrogate modeling workflow to solve rough surface contact simulations.

In this work, the performance of the trained surrogate models is evaluated on unseen but known test data (a subset of the database) using accuracy metrics, such as the mean square error (see Section 3.4).

Finally, in the fourth step, the surrogate model can be used to predict the quantity of interest for any new input point, for example during a multi-query analysis such as a parameter study or uncertainty quantification. This stage is referred to as the online phase. The first three steps (cf. Figure 10) take place in the offline phase, meaning they are performed only once.

The workflow is implemented in our in-house package called *DeepSim* (https://github.com/imcs-compsim/deep_sim), which is developed to automate numerical simulations, and machine learning frameworks. (The code will be available after acceptance)

3.2 Generation of Database

To generate the database, we first sample from the input parameter space and then run BEM simulations for each sample. The input space includes the statistical parameters of rough surfaces and the far-field displacement. As described in Section 2.1, the material properties do not influence the contact pattern. Therefore, parameters such as Young’s modulus and Poisson’s ratio are held constant throughout this study. Additionally, more samples are placed in regions of greater interest through controlled sampling [71]. The far-field displacement is sampled directly from the range $5\ \mu\text{m}$ to $45\ \mu\text{m}$, with a higher concentration of samples for $\Delta \leq 25\ \mu\text{m}$ (see Figure 11a and Figure 11b), since larger far-field displacements lead to prohibitive computational cost (cf. Figure 9). Statistical surface parameters are sampled indirectly: rough surfaces with a 128×128 grid are generated using the RMD algorithm (see Section 2.2), and their statistical properties

are computed as described in Section 2.3. BEM simulations are performed for each input sample to compute the corresponding effective contact area.

The resulting input-output pairs form the desired database. In total, we run 15,878 BEM simulations, with an average simulation time of 190 s per model evaluation. A comprehensive list of all parameters used in this study is provided in Table 1. The table includes fixed parameters (e.g., material and model parameters) used to generate the database, along with the observed ranges for all input and target quantities. The input features for the data-driven surrogate models consist of the far-field displacement and 22 statistical parameters describing the rough surfaces, as listed in Table 1. The database includes one quantity of interest, the effective contact area, which serves as the model output.

Note that the table presents raw data, before preprocessing (see Section 3.1). In particular, an L_2 -normalization is applied to ensure each feature vector has unit length:

$$X_i = \frac{x_i}{\sqrt{\sum_{i=1}^{n_f} x_i^2}}, \quad (9)$$

where x_i is the non-normalized feature, n_f is the number of features, and X_i is the normalized feature.

After preprocessing, the database is used to train fast-to-evaluate surrogate models. We adopt an 80:20 train-test split, resulting in a training set with 12,703 samples and a test set with 3,175 samples. Each sample has 23 features and one scalar target.

3.3 Fast-to-Evaluate Modeling with Hyperparameter Optimization

To find the optimal data-driven model, we compare different regression models, including Decision Tree [74], Random Forest [75], Support Vector Machine (SVM) Regressor [76], Adaptive Boosting (AdaBoost) [77], Gaussian Process (GP) Regressor [78], Gradient Boost [79], Kernel Ridge [80], eXtreme Gradient Boosting (XGBoost) [81], and Multi-Layer Perceptron (MLP) Regressor [82].

Figure 12 illustrates the classification of all the deployed machine learning algorithms based on their characteristics, categorized into three main

groups: tree-based models, kernel-based models, and neural networks.

Tree-based models are further divided into single and ensemble methods, depending on whether the model is a standalone decision tree or it is a combination of multiple decision trees. Boosting algorithms, on the other hand, sequentially construct ensemble algorithms to enhance prediction accuracy.

Kernel-based regression methods are non-parametric techniques that use kernel functions to map input data into high-dimensional feature spaces, allowing them to capture complex, nonlinear relationships. They leverage the *kernel trick* to compute inner products in the transformed space without explicitly performing the transformation [83]. Among the kernel-based models used, Kernel Ridge and SVM Regressors are deterministic, while the GP Regressor is probabilistic. When using the same kernel and hyperparameters, the mean prediction of a GP Regressor is equivalent to that of Kernel Ridge Regression (see Appendix A). The SVM Regressor aims to find a function (or hyperplane) that deviates from the actual target values by at most a specified margin (epsilon) for as many data points as possible, while also maintaining model simplicity (i.e., minimizing the norm of the weights).

The MLP Regressor, in contrast, is a neural network-based method capable of modeling nonlinear relationships through learned weights and activations. Note that the MLP Regressor with regularization and a single-layer architecture using a linear activation function and the Kernel Ridge algorithm employing a linear kernel exhibit similar characteristics.

Many machine learning models have hyperparameters. Hyperparameters are configuration settings that are set before training begins. They control the learning process (e.g., learning rate, batch size, number of layers) and significantly influence model performance but are not learned from the data. Since the choice of hyperparameters directly affects model accuracy and performance [84], we perform a hyperparameter optimization using grid search with cross-validation to identify the best-performing configuration of a model [85]. By comparing the best-performing configuration of each model, we ensure a fair comparison across models.

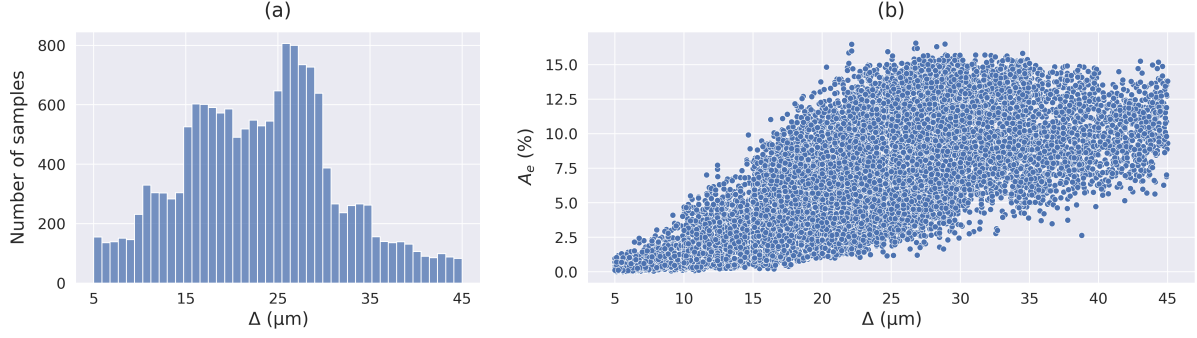


Fig. 11: Visualization of the database. (a) distribution of far-field displacement, and (b) scatter plot showing the target effective contact area against the feature far-field displacement. Each point represents a triplet consisting of a rough surface, a far-field displacement, and the corresponding effective contact area. Variations in effective contact area at a fixed far-field displacement are due to differences in the characteristics of the rough surfaces.

Table 1: The list of parameters of the generated raw database including material parameters, model parameters, statistical parameters, and the target quantity. Each row contains a parameter with corresponding symbol and the range of variation.

Type	Name	Symbol	Range
Model parameters	Scan length (μm)	L	1,000
	Hurst exponent (-)	H	[0.5, 0.8]
	Far-field displacement (μm)	Δ	[5, 45]
Statistical parameters	Mean of peaks (μm)	\bar{z}_p	[8.20, 47.51]
	Root mean square of peaks (μm)	$\text{RMS}[z_p]$	[2.54, 15.49]
	Kurtosis of peaks (-)	$\text{K}[z_p]$	[1.56, 7.13]
	Skewness of peaks (-)	$\text{Sk}[z_p]$	[-1.34, 1.36]
	Density of peaks (-)	ρ_p	[0.19, 0.27]
	Mean of curvature of peaks (μm^{-1})	$\bar{\kappa}_p$	[0.015, 0.066]
	Kurtosis of curvature of peaks (-)	$\text{K}[\kappa_p]$	[-0.07, 5.35]
	Skewness of curvature of peaks (-)	$\text{Sk}[\kappa_p]$	[0.55, 1.15]
	Bandwidth parameter in x direction (-)	α_x	[4.06, 46.19]
	Bandwidth parameter in y direction (-)	α_y	[4.19, 48.52]
	Mean of asperities (μm)	\bar{z}_a	[8.54, 48.18]
	Root mean square of asperities (μm)	$\text{RMS}[z_a]$	[2.56, 15.60]
	Kurtosis of asperities (-)	$\text{K}[z_a]$	[-1.45, 4.26]
	Skewness of asperities (-)	$\text{Sk}[z_a]$	[-1.34, 1.48]
	Density of asperities (-)	ρ_a	[0.08, 0.13]
	Mean of curvature of asperities (μm^{-1})	$\bar{\kappa}_a$	[0.017, 0.072]
	Root mean square of curvature of asperities (μm^{-1})	$\text{RMS}[\kappa_a]$	[0.007, 0.031]
Kurtosis of curvature of asperities (-)	$\text{K}[\kappa_a]$	[2.81, 15.14]	
Skewness of curvature of asperities (-)	$\text{Sk}[\kappa_a]$	[0.41, 1.6]	
Mean of surface height (μm)	\bar{z}	[7.71, 45.36]	
Max. of surface height (μm)	z^{max}	[16.36, 79.25]	
Root mean square of surface height (μm)	$\text{RMS}[z]$	[2.62, 15.55]	
Target parameter	Effective contact area (%)	A_e	[0.01, 16.56]

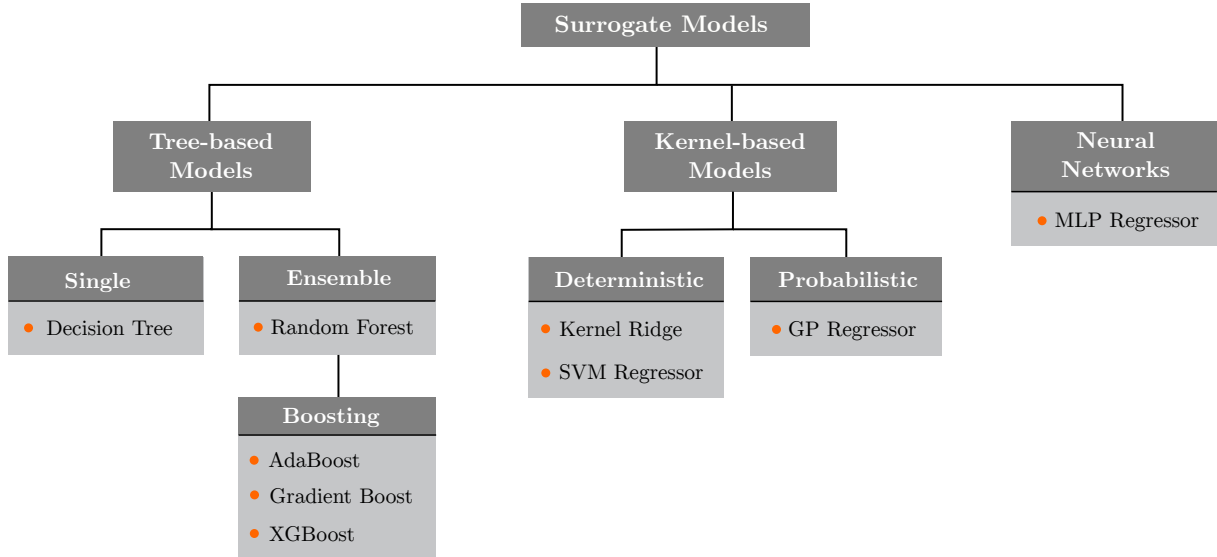


Fig. 12: Classification of surrogate modeling techniques based on their characteristics.

In a grid search, the model is trained on all combinations of hyperparameters on a predefined grid: First, a search space is specified for each hyperparameter. Second, the search space is sampled on a fixed number of grid points. Grid-based hyperparameter optimization suffers from the curse of dimensionality and can quickly become computationally very expensive. Despite its computational cost, we demonstrate that the effort is justified, as it leads to substantially improved model performance (cf. Section 4.2). To balance computational cost, we focus on tuning key hyperparameters only [84]. For example, in tree-based algorithms such as XGBoost, important hyperparameters include the learning rate, maximum tree depth, and the number of estimators, corresponding to the maximum number of boosting trees [86]. A full list of the investigated hyperparameters is provided in Table 2. Detailed descriptions of the machine learning models and their corresponding hyperparameters can be found in Pedregosa et al. [87].

To avoid setting aside a portion of the training data exclusively for validation (note that we already split the database into 80% training and 20% test data, cf. Section 3.2), we use k -fold cross-validation during hyperparameter optimization. This method splits the training data into k equal parts, or folds. The model is then trained

k times, each time using $k - 1$ folds for training and the remaining fold for validation. This ensures that every data point is used for both training and validation, providing a more reliable estimate of model performance. The final performance metric is obtained by averaging the results over all k runs. For more details on k -fold cross-validation, we refer readers to the original literature [88, 89]. In this study, we specifically apply 5-fold cross-validation.

Table 3 compares the computation times required for hyperparameter optimization across the models. Due to the curse of dimensionality, models with more hyperparameters generally require much longer tuning times. For instance, the Random Forest model involves evaluating 19,008 hyperparameter combinations ($9 \times 4 \times 11 \times 4 \times 3 \times 4 = 19,008$), as detailed in Table 2. In contrast, the Decision Tree and MLP Regressor models involve fewer combinations—600 and 756, respectively. However, the MLP Regressor still requires significantly more tuning time due to the higher training cost per configuration. Unlike Decision Trees, MLPs must learn additional internal parameters, such as weights and biases, for each hyperparameter setting [82]. In total, hyperparameter tuning for the MLP Regressor takes over 12 h, whereas for the Decision Tree model it takes only about 16s, a negligible amount by comparison.

Table 2: Investigated surrogate model hyperparameter optimization, including the model type, selected hyperparameters, the defined parameter search space, and the optimal parameter value.

Model	Hyperparams.	Search space	Grid points	Optimum
Decision Tree	max depth	1 - 30	5	30
	max features	auto, sqrt, log2, none	4	none
	min samples leaf	1 - 15	6	7
	min samples split	2 - 10	5	10
Random Forest	max depth	5 - 100	9	20
	max features	sqrt, log2, 0.3, 1	4	1
	# estimators	20 - 2,000	11	1,000
	criterion	sq. err., abs. err., Friedman, Poisson	4	sq. err.
	min samples split	2 - 10	3	2
	min samples leaf	1 - 15	4	1
AdaBoost	max depth	3 - 35	7	18
	loss	linear, square, exponential	3	square
	# estimators	10 - 1500	11	1,500
	learning rate	1×10^{-2} - 2.0	9	1.0
Gradient Boost	learning rate	1×10^{-3} - 2.0	8	0.05
	loss	sq. err., abs. err., huber, quantile	4	sq. err.
	max depth	5 - 100	8	5
	# estimators	50 - 1,600	10	1,600
	criterion	Friedman, sq. err.	2	Friedman
	max features	auto, sqrt, log2	3	auto
XGBoost	learning rate	1×10^{-2} - 2.0	8	0.1
	max depth	3 - 15	5	3
	# estimators	10 - 1,500	14	1,500
	gamma	0 - 2	8	0.0
SVM Regressor	C	0.1 - 1,400	12	1,400
	degree	3 - 7	3	7
	kernel	linear, rbf, poly, sigmoid	4	poly
	gamma	scale, auto	2	scale
	cache size	200 - 5000	6	200
GP Regressor	alpha	1×10^{-3} - 1.0	110	0.0374
Kernel Ridge	alpha	1×10^{-5} - 1	8	1×10^{-5}
	gamma	0.01 - 150	10	5
MLP Regressor	kernel	rbf, linear	2	rbf
	activation	logistic, relu, tanh	3	tanh
	alpha	1×10^{-4} - 5×10^{-3}	7	1×10^{-3}
	hidden layer sizes	nodes: 50 - 120, 2-4 layers	4	[50, 100, 200, 100, 50]
	learning rate	constant, invscaling, adaptive	3	adaptive
	solver	sgd, adam, lbfgs	3	lbfgs

Table 3: Assessment of time required for performing hyperparameter optimizations.

	Decision Tree	Random Forest	AdaBoost	Gradient Boost	XGBoost	SVM Regressor	GP Regressor	Kernel Ridge	MLP Regressor
Tuning time (s)	16	1,628,304	42,814	900,946	120,845	25,120	61,494	2,599	44,325

3.4 Accuracy Metrics

To evaluate the performance of the models, four metrics are introduced: normalized mean square error (nMSE), normalized mean absolute error (nMAE), normalized max-error (nMaxE), and the R^2 score [90]. Accuracy metrics without normalization are scale-dependent [91]. In other words, scale-dependent measures always require information about the scale of the target to assess the model’s accuracy effectively. For the following expressions of normalized metrics, A_e denotes the ground truth, \hat{A}_e is the prediction, \bar{A}_e is the mean ground truth of the test data, $\max(|A_e|)$ is the max value of ground truth in the test data, and n is the number of test points.

The normalized mean square error (nMSE) is defined as:

$$\text{nMSE} = 100 \frac{\frac{1}{n} \sum_{i=1}^n (A_e^i - \hat{A}_e^i)^2}{\bar{A}_e} \%. \quad (10)$$

The nMSE metric quantifies the average squared differences between predictions and ground truths, normalized by the mean of the ground truth. Since it penalizes larger errors more heavily, it is particularly sensitive to outliers. A lower nMSE indicates a better model fit.

The normalized mean absolute error (nMAE) is formulated as:

$$\text{nMAE} = 100 \frac{\frac{1}{n} \sum_{i=1}^n |A_e^i - \hat{A}_e^i|}{\bar{A}_e} \%. \quad (11)$$

The nMAE metric measures the average absolute differences between predictions and ground truths, providing an interpretable error metric. Unlike nMSE, nMAE treats all errors equally and is more robust to outliers. Lower nMAE values indicate higher prediction accuracy.

The normalized max-error (nMaxE) is expressed as:

$$\text{nMaxE} = 100 \frac{\max(|A_e - \hat{A}_e|)}{\max(|A_e|)} \%. \quad (12)$$

The nMaxE metric captures the largest absolute error relative to the maximum observed value in

the test data. It highlights the worst-case error scenario, making it useful for applications where large deviations are critical. A lower nMaxE suggests that the model avoids large prediction errors.

The R^2 metric, also referred to as the coefficient of determination, quantifies how well the predictions match with actual values. Usually, the R^2 value ranges from 0 to 1, or from 0% to 100%. The accuracy metric R^2 is defined as

$$R^2 = 100 \left[1 - \frac{\sum_{i=1}^n (A_e^i - \hat{A}_e^i)^2}{\sum_{i=1}^n (A_e^i - \bar{A}_e)^2} \right] \%. \quad (13)$$

R^2 measures the proportion of variance in the actual values that is explained by the model predictions. A value close to 100% indicates a strong predictive model, while lower values suggest poor explanatory power.

Accuracy metrics are utilized for quantifying the investigated surrogate models based on the predicted and actual effective contact area. Also, note that all metrics are unitless and defined as percentages.

4 Results and Discussion

4.1 Evaluation of Baseline Models

The evaluation of the so-called baseline models aims to compare the investigated machine learning algorithms without hyperparameter optimization in terms of accuracy metrics, fit, and prediction time on unseen test data.

Figure 13 shows the qualitative comparison of the investigated baseline models to predict the effective contact area. Each figure has a red line, also referred to as the perfection line, which is used to qualify the model prediction. The qualitative accuracy of the model can be determined by how closely its predictions align with the red curve. A simple tree-based method such as Decision Tree shows a linear trend that is consistent with the perfection line. However, it exhibits a high variance, which causes a bad generalization. On the other hand, ensemble methods that rely on multiple decision trees, such as Random Forest, Gradient Boost, and XGBoost, exhibit reduced variance, thus leading to improved accuracy. While the majority of ensemble methods

perform well, AdaBoost stands out as a negative exception. The AdaBoost algorithm struggles to grasp the underlying patterns in the data, often delivering the same predictions although the actual values are different, thus indicating potential underfitting.

The SVM Regressor deviates slightly from the perfection line with an increasing variance for larger values of the effective contact area. In cases where the target values are small, the SVM Regressor tends to produce some negative, physically unrealistic predictions (the effective contact area can not take negative values). Similarly, the Kernel Ridge algorithm excessively deviate from the perfection line, predicting large negative values of the effective contact area even though the actual values are meant to be small yet positive. These noticeable deviations around small effective contact area values can be related to the dominating effect of the loss function contributions of data points with large effective contact area values during training. Since the Kernel Ridge algorithm is not yet tuned and has a simple model complexity, it tends to prioritize minimizing errors for larger values, which is why we observe significant deviations around the small effective contact values. On the other hand, the MLP Regressor with a single hidden layer using the rectified linear unit (relu) activation function demonstrates a behavior similar to that of the SVM Regressor, In particular, it tends to predict comparably large negative values of the effective contact area around the origin. However, in contrast to the SVM Regressor, exhibits significantly lower variance, especially for larger effective contact areas. The GP Regressor model outperforms all other baseline models in terms of accuracy and exhibits comparably reduced variance around the perfection line.

Figure 14a provides a quantitative comparison of accuracy metrics, namely nMSE (%), nMAE (%), nMaxE (%), and the R^2 score (%) for the investigated baseline models. Since the Decision Tree algorithm by definition mimics the training data, it yields 0% nMSE, nMAE, nMaxE along with 100% R^2 in the training data set. However, it suffers from a relatively high nMaxE value in the test data, e.g., nMaxE = 24.62%. The corresponding numbers for nMSE, nMAE, nMaxE and R^2 are provided in Table 4. The large difference between train and test metrics means that the baseline model based on the Decision Tree can not

properly generalize the problem. Yet, the Decision Tree model has the fastest prediction and fit times as depicted in Figure 14b. The Random Forest exhibits smaller test errors in terms of nMSE and nMAE compared to nMaxE and it does not indicate any sign of overfitting. However, it has the largest fit time of $t_f = 19.99$ s. Similarly, the SVM Regressor exhibits larger nMaxE values when compared to other accuracy metrics and it has the largest prediction time with $t_p = 3.408$ s. The Kernel Ridge model produces the largest test errors in the test data with nMSE = 19.11%, nMAE = 13.02%, and nMaxE = 34.45%. Moreover, it has a poor performance in terms of R^2 . The ensemble method AdaBoost also produces large test errors and has the poorest coefficient of determination of $R^2 = 90.71\%$. Other ensemble methods such as Gradient Boost and XGBoost demonstrate better results in general. Additionally, XGBoost has the second-fastest fit and prediction time, following closely after the Decision Tree. As a neural network model, MLP Regressor produces smaller test errors in terms of nMSE and nMAE, but it has the largest fit time with $t_f = 12.88$ s. Among all the investigated methods, the GP Regressor model stands out for its exceptional performance when considering various accuracy metrics in test data, e.g., nMSE = 1.15%, nMAE = 3.05%, and nMaxE = 11.76% along with $R^2 = 99.53\%$.

4.2 Evaluation of Tuned Models

As mentioned earlier, hyperparameter optimization or tuning is a crucial and necessary step to improve model performance and the ability to generalize from seen to unseen data. Also, tuning can reduce prediction and fit times. Figure 15 qualitatively illustrates the comparison of baseline models and tuned models with their respective predictions of the effective contact area. For all investigated models, there is a drastic improvement in accuracy. Particularly for AdaBoost, SVM Regressor, Kernel Ridge, and MLP Regressor models, predictions now closely align with the perfection line in contrast to the baseline models. Furthermore, the tuned models are quite effective in avoiding unphysical negative values for the effective contact area, particularly for the Kernel Ridge, the SVM Regressor and the MLP Regressor.

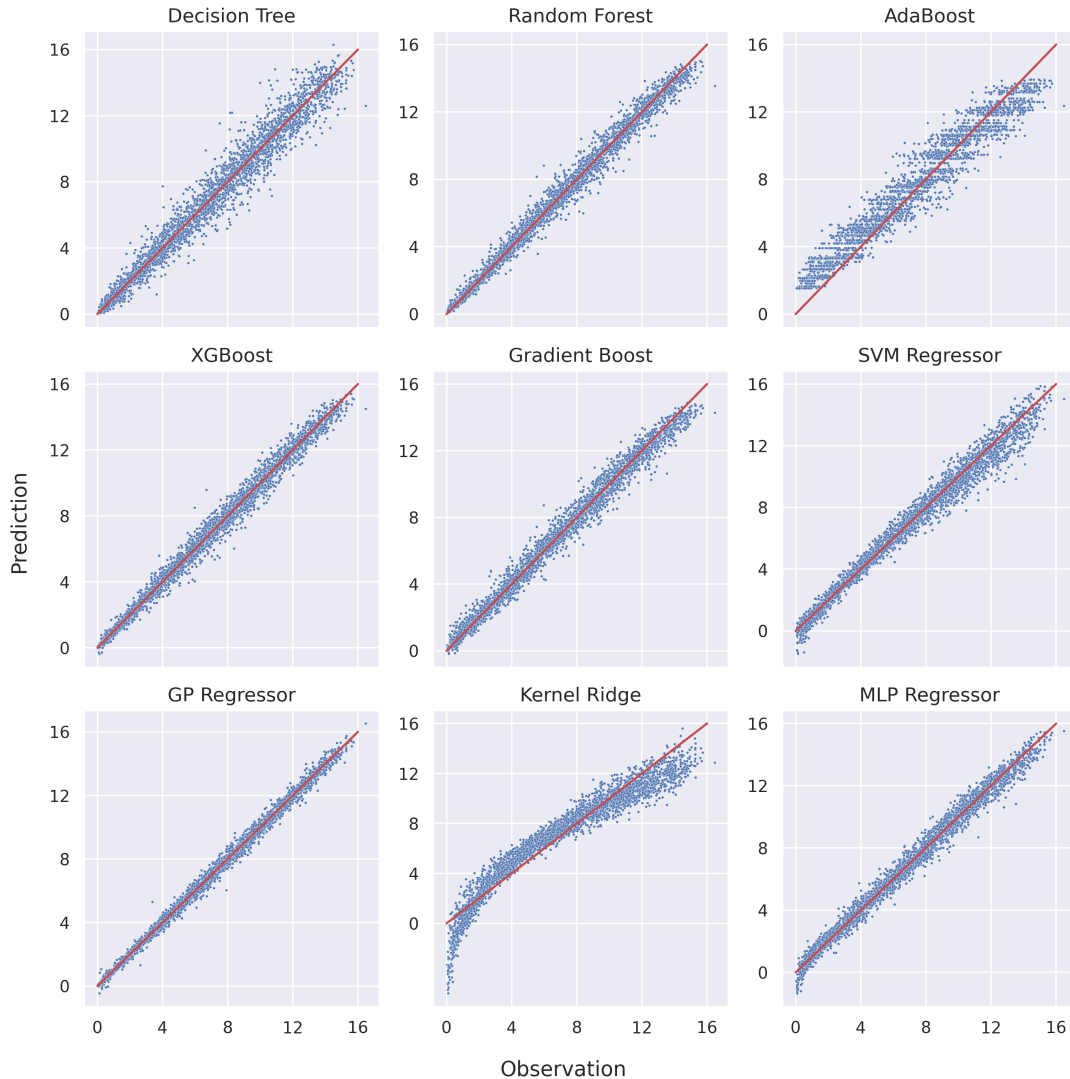


Fig. 13: Comparison of the investigated baseline models to predict the effective contact area (%). Horizontal axes are the observations or actual values, while vertical axes denote the predictions. The red lines represent a perfect fit, which is used to qualify the model’s accuracy.

Table 4 provides quantitative comparisons of baseline and tuned models in terms of accuracy metrics and computational time for model fitting and prediction. Hyperparameter optimization yields varying improvements across models, often at the expense of increased training time. For both the Decision Tree and Random Forest models, tuning yields slight improvements in most accuracy metrics, except for nMaxE. Specifically, for the Decision Tree, the prediction time remains almost the same, while the

fit time decreases slightly from 0.48s to 0.42s. Conversely, the Random Forest model shows a drastic increase in both training and prediction time, nearly 15 times larger. The fit time increases dramatically from 19.99s to 298.58s and the prediction time rises from 0.094s to 1.364s. The tuned SVM Regressor demonstrates remarkable performance improvements, with nMSE decreasing from 5.47% to 1.20%, nMAE from 6.50% to 3.09%, and nMaxE from 22.30% to 10.62%, while the R^2 value increases from 97.61% to

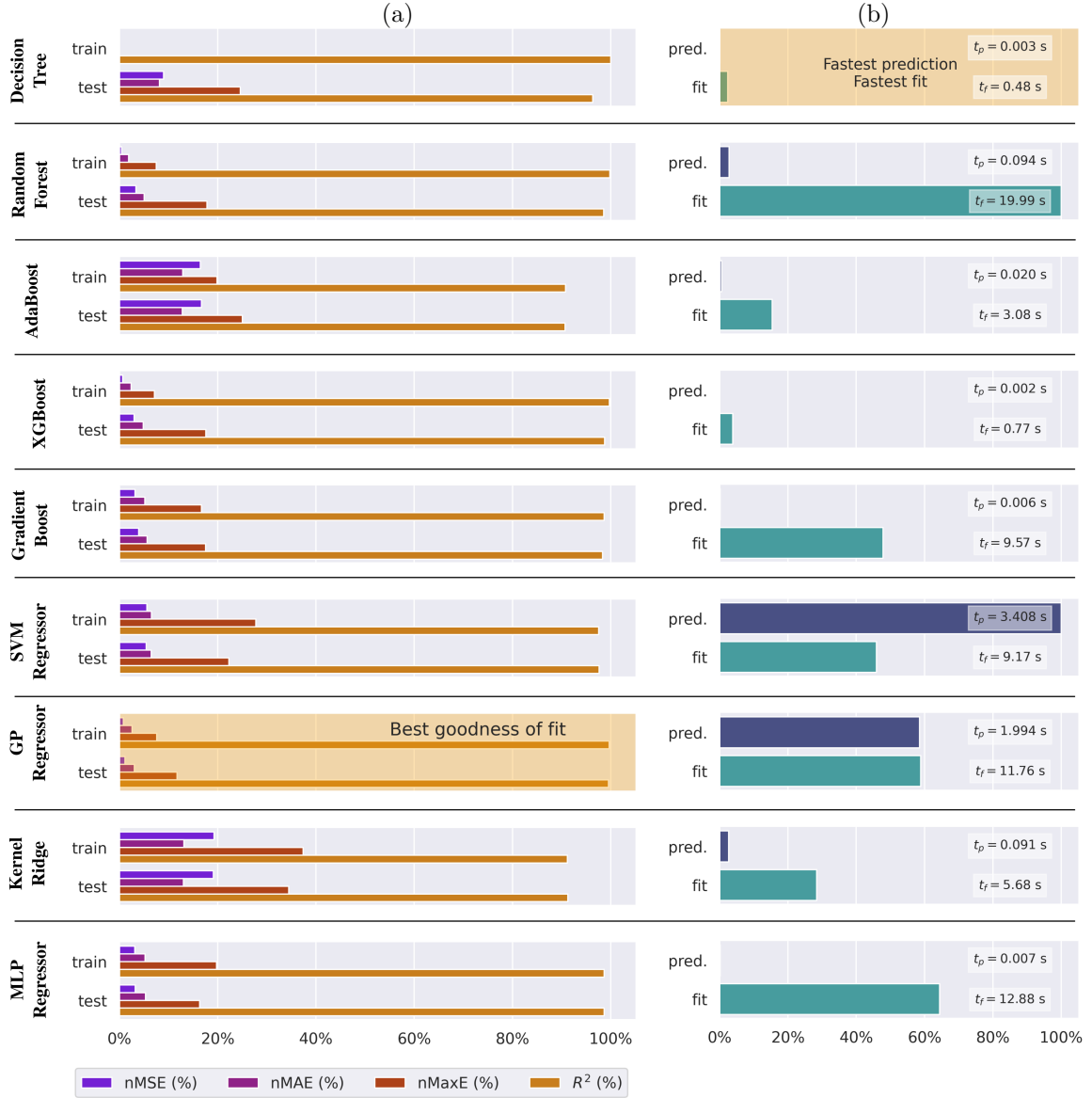


Fig. 14: Comparison of the investigated data-driven baseline models to predict the effective contact area for rough surface contact: (a) Accuracy metrics (%), (b) times for fit and prediction in % are given including the corresponding actual values in s. Note that each accuracy metric is scaled relative to the worst accuracy across all models to enable better comparisons. Similarly, each prediction and fit time measures are scaled relative to the maximum prediction and fit time across all models.

99.50%. However, these gains come with a steep computational cost, as the fit time increases from 9.17s to 2,550s. Yet, the tuned SVM Regressor model exhibits a reasonable reduction in prediction time. Tuned ensemble methods, e.g., AdaBoost, Gradient Boost, and XGBoost, exhibit great improvements in accuracy metrics with

an average improvement factor of approximately 40%. Among the ensemble approaches, the tuned XGBoost model demonstrates outstanding computing performance, delivering a fit time of $t_f = 4.13$ s and a prediction time of $t_p = 0.005$ s.

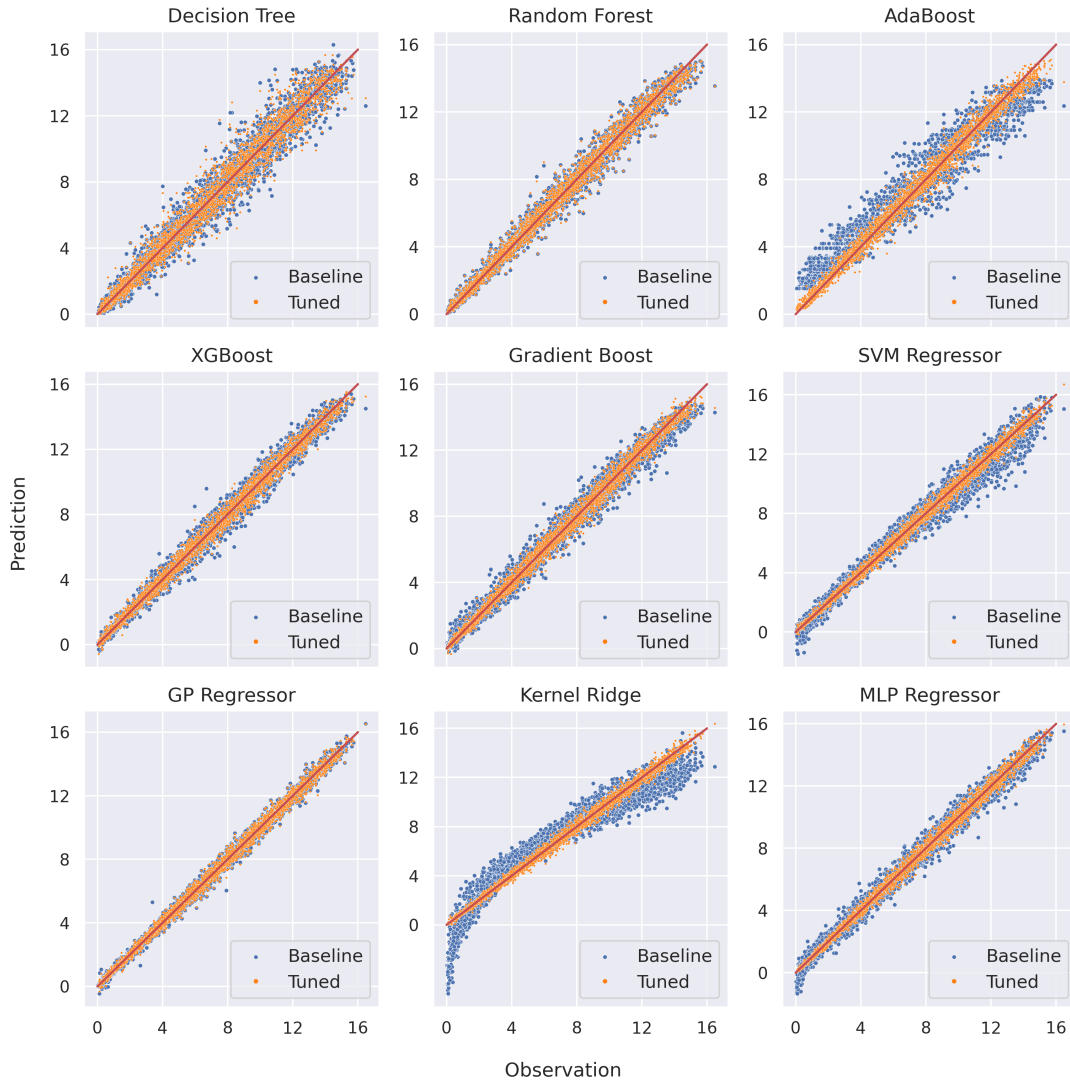


Fig. 15: Comparison of the baseline models with the tuned models. Horizontal axes represent the observations or actual values, while vertical axes denote the predictions. The red lines represent a perfect fit, which is used to qualify the model’s accuracy.

The tuned MLP Regressor model exhibits better goodness of fit than the tree-based models across all accuracy metrics, with $nMSE = 1.19\%$, $nMAE = 3.09\%$, $nMaxE = 9.95\%$, and $R^2 = 99.51\%$. With these values, it ranks as the third-best model overall in terms of accuracy. However, training the tuned MLP Regressor requires approximately 3,435 s, making it the most time-consuming training process among all models. The fit time is approximately 266 times longer than that of the baseline model, primarily due to

a significantly higher number of training epochs and increased model complexity. Specifically, the tuned model is trained over 20,000 epochs, compared to just 200 epochs for the baseline. In addition, the tuned MLP employs a deeper architecture with more neurons and layers, resulting in a substantially larger number of internal parameters to optimize. With a prediction time of 0.049 s, the MLP Regressor lies in the middle range. It is an order of magnitude slower than the Decision Tree, yet two orders of magnitude faster than

the slowest models, such as the GP Regressor and Random Forest.

For the GP Regressor model, tuning leads to slight improvements in nMSE and nMAE, and a substantial reduction in nMaxE—from 11.76% to 8.98%. As a result, the GP Regressor achieves the best overall accuracy across all evaluated metrics, making it the most effectively tuned model in this study. However, this gain in accuracy comes at a considerable computational cost: the fit time increases sharply from 11.76 s to 853.23 s, representing more than a 70-fold increase, while the prediction time remains nearly unchanged. A significant portion of this fit time is spent on computing the maximum likelihood estimation of the kernel parameters. In contrast, the tuned Kernel Ridge model delivers accuracy metrics comparable to those of the GP Regressor, but with much lower computational demands—requiring only 9.18 s for training and 0.827 s for prediction. Overall, we consider the tuned Kernel Ridge model to be the most balanced surrogate, as discussed in Section 4.5. For this reason, we focus on this model in greater detail in the following sections.

4.3 Evaluation of Kernel Ridge on a Fine Grid

As explained in Section 3.2, the database is generated with rough contact simulations on a 128×128 grid. Correspondingly, surrogate models are trained using the statistical features that are obtained from these relatively coarse grids. The question naturally arising here is whether it would be possible to predict the effective contact area resulting from a finer grid, e.g., 256×256 points per side, using the surrogate Kernel Ridge model, which has been trained on a database whose features are extracted exclusively from samples having a coarser grid, namely 128×128 . To answer this question, 800 additional BEM simulations based on a 256×256 grid are run. Following the same process as explained in Section 3.2, a database for testing is generated including model parameters and statistical parameters based on the fine grids, and predictions are computed using the already trained Kernel Ridge model. As depicted in Figure 16a, the predicted effective contact area via Kernel Ridge aligns nicely with the actual values obtained through the BEM model, which is

also confirmed by the computed accuracy metrics as provided in Table 5. Indeed, compared to the coarser BEM grids, the computed accuracy metrics are slightly different, since no information from finer grids is used during the model training. In terms of evaluation or prediction time, the surrogate model is more efficient and the gap between Kernel Ridge and BEM increases drastically since simulations with the finer grid take extensively longer computing time.

4.4 Comparative Cost Analysis of Reference and Surrogate Models

The motivation behind building surrogate models is to construct fast-to-evaluate approximations of the BEM reference model, thereby making multi-query scenarios, requiring numerous model evaluations, computationally tractable. While surrogate models reduce evaluation time compared to the reference model, they also introduce additional upfront costs associated with model construction.

Ultimately, our goal is to determine the break-even point, the number of model evaluations at which the computational savings from using the surrogate outweigh the cost of building it. To analyze this, we conduct a comparative cost analysis of the overall computational cost of using the Kernel Ridge model versus the reference numerical method (BEM) for an increasing number of simulations. For the BEM model, the total cost t_{BEM} is obtained by summing the time required for each individual simulation. As shown in Figure 9, the simulation time depends on both surface properties and the applied far-field displacement. Therefore, the exact cost of a specific BEM simulation is not known in advance. To approximate the total cost, we use the average simulation time from the database generation process, which is 189.79 s. This average is assumed to be a reliable estimate of expected cost, especially when considering a large number of simulations.

In contrast, computing the total cost for the surrogate model is more intricate. To ensure a fair comparison, all components of the surrogate modeling process must be considered. Specifically, we account for four time contributions involved in building and using the surrogate model. The first contribution is the model evaluation time, which refers to the total cost t_p of making predictions

Table 4: Comparison of the baseline models with the tuned models. Accuracy metrics nMSE, nMAE, nMaxE, R^2 are evaluated on the test data. Improvement is calculated based on $100(m_t - m_b)/m_b$ where m_b is the evaluated performance metric of the baseline model and m_t is the evaluated performance metric of the tuned model. The cells with blue background show the model accuracy of the best baseline model, the cells with orange background denote those of the best-tuned model, while the cells with green background show the model accuracy and performance of the model considered "optimal" overall. The model accuracy is determined based on accuracy metrics, and the model performance is assessed by examining fit and prediction time. The fit (or training) time refers to the time required to train the models on the training dataset, whereas the prediction time is measured on the test dataset and represents the total time needed to make predictions for all test data points.

		Performance metric (%)				Time (s)	
		nMSE	nMAE	nMaxE	R^2	fit (t_f)	pred. (t_p)
Decision Tree	Baseline	8.99	8.17	24.62	96.31	0.48	0.003
	Tuned	8.51	8.03	27.66	96.51	0.42	0.003
	Improvement	5.34	1.71	-12.35	0.21		
Random Forest	Baseline	3.39	5.05	17.81	98.56	19.99	0.094
	Tuned	3.34	5.01	18.58	98.58	298.58	1.364
	Improvement	1.47	0.79	-4.32	0.02		
AdaBoost	Baseline	16.71	12.80	25.03	90.71	3.08	0.020
	Tuned	2.92	4.77	16.34	98.76	230.11	1.174
	Improvement	82.53	62.73	37.72	8.87		
XGBoost	Baseline	3.01	4.86	17.59	98.75	0.77	0.002
	Tuned	1.95	4.03	10.34	99.19	4.13	0.005
	Improvement	35.22	17.08	41.25	0.45		
Gradient Boost	Baseline	3.95	5.68	17.55	98.30	9.57	0.006
	Tuned	2.03	4.03	11.55	99.15	197.10	0.067
	Improvement	48.61	29.05	34.19	0.86		
SVM Regressor	Baseline	5.47	6.50	22.30	97.61	9.17	3.408
	Tuned	1.20	3.09	10.62	99.50	2550.27	0.624
	Improvement	78.06	52.46	52.38	1.94		
GP Regressor	Baseline	1.15	3.05	11.76	99.52	11.76	1.994
	Tuned	1.12	3.02	8.98	99.54	853.23	1.965
	Improvement	2.61	0.98	23.64	0.02		
Kernel Ridge	Baseline	19.11	13.02	34.45	91.24	5.68	0.091
	Tuned	1.16	3.07	9.84	99.52	9.18	0.827
	Improvement	93.93	76.44	71.44	9.07		
MLP Regressor	Baseline	3.24	5.32	16.34	98.64	12.88	0.007
	Tuned	1.19	3.09	9.95	99.51	3435.54	0.049
	Improvement	63.27	41.92	39.11	0.88		

using the surrogate model across all input samples. To accurately estimate the prediction time for a single sample, we compute the average prediction time based on 2,000 randomly selected input samples, drawn uniformly from the feature

ranges specified in Table 1. The second contribution is the fit time t_f , i.e., the time required to train the surrogate model on the available training data. The third contribution is the cost of hyperparameter optimization t_h , which, as shown

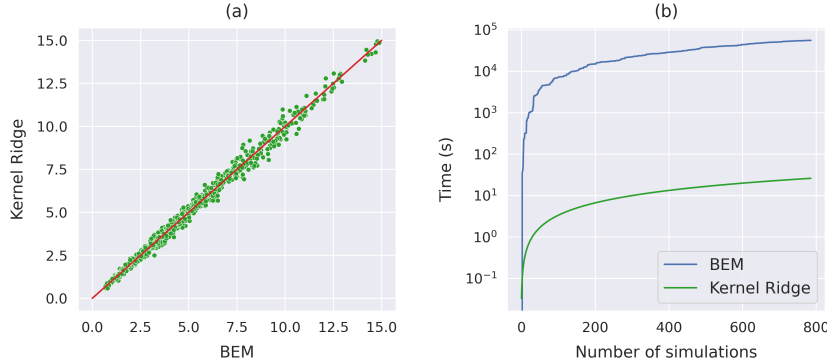


Fig. 16: Comparison of the Kernel Ridge and the BEM model in terms of (a) effective contact area, (b) evaluation or prediction time. Rough surfaces are characterized by a 256×256 grid.

in Table 3, can be substantial. Finally, we include the cost of generating the database t_d , as this is a necessary prerequisite for training any surrogate model. This includes both the generation of input samples (e.g., synthetic surfaces and far-field displacements) and the corresponding evaluations using the reference BEM model to obtain the output quantities. The total cost of the Kernel Ridge Regressor can finally be computed as $t_{KRR} = t_p + t_f + t_h + t_d$.

A visualization of the comparative computational cost analysis is provided in Figure 17. The overall cost of using the surrogate model is dominated by the database generation time t_d , which is several orders of magnitude greater than the other cost components. The model training time is negligible: on average, a single BEM evaluation is more expensive than the combined cost of training and evaluating the Kernel Ridge model. Even the hyperparameter optimization step, while computationally intensive within the surrogate modeling workflow, contributes only marginally when compared to the cost of evaluating the reference model. Its cost breaks even after just 14 model evaluations, including both training and prediction. A comparison of the total costs, t_{BEM} and t_{KRR} , shows that the break-even point is reached at approximately 15,893 simulations. In other words, the surrogate model becomes the more cost-efficient choice only when more than this number of simulations is required. It is noteworthy that the database used to train the surrogate model consists of 15,878 samples,

further underscoring the dominant cost associated with generating training data. Essentially, all other surrogate-related costs, including evaluation, training, and tuning times, are negligible in comparison. Although the break-even may initially seem like a high threshold, it is important to consider that applications such as uncertainty quantification (UQ) and Bayesian parameter calibration often involve several tens of thousands of model evaluations [64]. In such scenarios, the break-even point can be reached relatively quickly, making surrogate modeling a practical and cost-effective solution.

4.5 Discussion

In Section 4.1 and Section 4.2, the investigated surrogate models were compared in terms of accuracy-using standard metrics-and in terms of performance, based on model fit and prediction times. Our findings suggest that selecting an optimal surrogate model requires balancing accuracy with prediction performance, depending on the specific requirements of the application task. While the optimal choice is task-dependent, several general trends can be observed.

Tree-based models, such as Decision Trees and Random Forests, typically perform worse in terms of accuracy compared to kernel-based methods. However, they offer significantly faster prediction times. This makes them suitable candidates in scenarios where rapid evaluations are critical and minor accuracy trade-offs are acceptable-such

Table 5: Corresponding accuracy metrics.

Metric (%)	Value
nMSE	1.46
nMAE	3.95
nMaxE	7.56
R^2	99.16

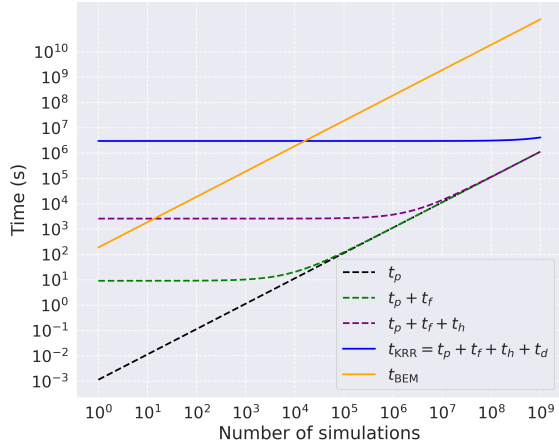


Fig. 17: Comparison of the total computational cost for the BEM model and the Kernel Ridge surrogate model. For BEM, the cost is estimated using the average simulation time (189.79 s) per sample. The surrogate model cost includes four components: prediction time (t_p), training time (t_f), hyperparameter optimization time (t_h), and database generation time (t_d), with total cost $t_{\text{KRR}} = t_p + t_f + t_h + t_d$. The surrogate model’s overall cost is dominated by database generation (t_d), while training and hyperparameter optimization contribute marginally. The surrogate becomes more cost-efficient than BEM after approximately 15,893 simulations.

as in real-time applications. In contrast, kernel-based models achieve superior accuracy. Although their prediction times are generally higher than tree-based models, they are still relatively low in absolute terms (on the order of seconds for 3,175 test points), making them viable for most practical applications. Among the kernel-based models, the GP Regressor yields the best accuracy metrics, closely followed by the Kernel Ridge model. The differences in accuracy between these two models are negligible for most practical purposes. However, the GP Regressor has approximately twice the prediction time of the Kernel Ridge model. This is expected, as the GP Regressor also provides a predictive variance alongside the mean estimate—an added value that explains the increased computational cost. If uncertainty quantification is not required, the Kernel Ridge model provides nearly identical predictions at half of the computational cost. This is not surprising,

as both methods are closely related. In fact, the mean prediction of the GP Regressor is mathematically equivalent to that of the Kernel Ridge model, provided the same hyperparameters are used—namely, the kernel type, kernel parameters, and regularization parameter. The MLP Regressor, while slightly less accurate than the Kernel Ridge model, achieves lower prediction times—around one order of magnitude faster. However, this comes at the expense of a significantly longer training time and increased model complexity.

Overall, the tuned Kernel Ridge model offers the best trade-off between accuracy and computational efficiency. It delivers high prediction accuracy with low prediction times and minimal training overhead, making it a strong candidate for general-purpose surrogate modeling. Therefore, while the GP Regressor achieves the highest accuracy, it is not considered the optimal model due to its substantially longer fit time and higher prediction cost. The tuned Kernel Ridge model is identified as the most balanced surrogate for a wide range of application scenarios.

In Section 4.4, we compared the overall costs of using a surrogate model with those of the reference model. Our results highlight that a fair comparison between data-driven surrogate models and reference models can only be made by considering the total cost—including both offline and online phases. The reasoning behind this is as follows: A general machine learning regression task aims to learn an unknown functional relationship from input-output data. It is common practice to distinguish between the offline and online phases of model development, as they typically involve different tasks and cost structures [72]. The offline phase includes data generation (collection, preprocessing, and feature selection) and model training. The online phase refers to the cost of evaluating the trained model. This separation is particularly relevant because online applications often involve a large number of model evaluations, while offline processes are performed only once. As a result, the substantial cost of the offline phase is usually justified as a one-time investment to obtain a usable model in the first place.

However, unlike standard machine learning scenarios where no prior model exists, surrogate modeling assumes the existence of a reliable reference model—typically one that is accurate but computationally expensive. The surrogate’s

purpose is to approximate this reference model efficiently, enabling its use in applications such as optimization, uncertainty quantification (UQ), or parameter identification, where many evaluations are required. In these contexts, the total cost of using a surrogate model—including both offline and online phases—must be considered to fairly assess its efficiency in solving the application task. Solving the task with the reference model involves direct evaluation across many configurations, often resulting in high computational cost. In contrast, the surrogate model approach requires an initial investment: building the surrogate entails data generation, model training, and hyperparameter tuning. Once constructed, the surrogate is then evaluated across the same configurations as the reference model, but at significantly lower cost per evaluation. Ultimately, the initial cost of building a surrogate is incurred specifically for the application task at hand. Therefore, the offline cost must be included in the overall assessment of the surrogate model’s efficiency. Our results demonstrate that ignoring the offline costs leads to a distorted assessment, which falsely overstates the advantages of data-driven modeling. Comparing only the evaluation times of the models, as it is often done in the literature, is insufficient, since it neglects the largest cost component: database generation. However, the encouraging finding is that there is no practical need to rely on such an incomplete or unfair comparison. Even though the break-even point may initially appear high, our analysis shows that the proposed surrogate modeling approach remains highly worthwhile for many application tasks that involve large numbers of model evaluations.

5 Conclusion

In this study, we developed a surrogate modeling framework to predict the effective contact area in rough surface contact problems involving a linear elastic half-space and a rigid rough surface. A comprehensive database was constructed using BEM simulations, containing far-field displacements, 22 statistical parameters derived from synthetic surface height fields, and the target output—the effective contact area. Several machine learning regression models were evaluated as surrogate modeling techniques. Optimal model configurations were determined through hyperparameter optimization

using grid search with cross-validation. All models were assessed using standard accuracy metrics, as well as training and prediction times to evaluate their computational performance.

Our findings indicate that selecting an optimal surrogate model requires balancing predictive accuracy and computational performance, depending on the specific requirements of the application task. Each model exhibits distinct characteristics, meaning that the ideal choice is context-dependent—for instance, a model prioritizing speed may be preferred in time-critical applications, whereas a more accurate model might be favored in precision-sensitive tasks. Overall, our results show that the Kernel Ridge model offers the most favorable trade-off between accuracy and efficiency across a broad range of scenarios. It achieves high accuracy, low prediction time, and minimal training overhead, making it a strong candidate for general-purpose surrogate modeling. The Gaussian Process Regressor presents a compelling alternative when uncertainty quantification is required, although it incurs a higher computational cost due to variance estimation. To assess the robustness of the surrogate modeling approach, the generalization capability of the Kernel Ridge was evaluated on previously unseen simulation scenarios. The results demonstrate that the surrogate model maintains reliable predictive accuracy and computational efficiency even when applied beyond the resolution used during training, highlighting its potential for broader applicability. When evaluating the effectiveness of the surrogate modeling approach, the break-even point—where the overhead of building the surrogate is offset by its reduced evaluation cost—is of particular interest. We emphasize the importance of accounting for all offline costs, especially database generation. Neglecting these costs, as is sometimes done in the literature, results in a skewed evaluation that overstates the benefits of data-driven modeling. Nonetheless, we conclude that such an incomplete assessment is unnecessary in practice. Even though the break-even point may initially appear high, the proposed surrogate modeling framework proves to be highly beneficial for many application scenarios that involve large numbers of model evaluations.

To conclude, the identified Kernel Ridge surrogate model predicts the effective contact area with acceptable accuracy and robustness while

significantly reducing evaluation time compared to state-of-the-art numerical methods such as the Boundary Element Method (BEM). As such, it serves as an attractive and efficient surrogate for use in multi-query analyses, such as uncertainty quantification, parameter identification, and sensitivity analysis.

This work reveals several opportunities for further investigations. Apart from statistical parameters, only the far-field displacement has been considered as input for the surrogate modeling strategy. However, the input space could be extended to other properties, e.g., geometrical parameters such as the scan length. Moreover, not only the effective contact area but also the overall contact force could be considered as relevant model output to formulate and solve the problem as a multi-target regression task. As an alternative approach, the contact force field can be predicted using a neural network approach consisting of both fully connected and convolutional neural networks, by taking contour plots of the topographies as image-based input and far-field displacement values as numerical input. Eventually, the proposed surrogate modeling framework could be formulated as a hybrid model that combines data-driven components and model-based approaches that include the physics of the underlying problem.

Declarations

Availability of data and materials

The datasets generated and analysed during the current study, as well as the source code, are publicly available at <https://github.com/imcs-compsim/deep-sim>.

Competing interests

The authors declare that they have no competing interests.

Funding

This research paper is funded by dtec.bw - Digitalization and Technology Research Center of the Bundeswehr (project RISK.twin). dtec.bw is funded by the European Union - NextGenerationEU.

Acknowledgments

The authors gratefully acknowledge the computing resources provided by the Data Science & Computing Lab at the University of the Bundeswehr Munich.

Appendix A Comparison of GP Regressor and Kernel Ridge

In the kernel-based regression, the predicted output \hat{y} is calculated as

$$\hat{y} = \sum_{i=1}^N \alpha_i \kappa(\mathbf{x}, \mathbf{x}_i), \quad (\text{A1})$$

where α is the dual parameter, κ is the kernel function and N denotes number of sample points. The dual parameters for both models are calculated as

$$\begin{aligned} \alpha &= (\mathbf{K} + \sigma_n^2 \mathbf{I})^{-1} \mathbf{y} \rightarrow \text{GP Regressor} \\ \alpha &= (\mathbf{K} + \lambda \mathbf{I})^{-1} \mathbf{y} \rightarrow \text{Kernel Ridge} \end{aligned}$$

where \mathbf{K} is the kernel matrix, λ is the regularization term, \mathbf{I} is the identity matrix, and σ_n^2 is the noise variance. As long as the same kernel function with identical kernel parameters is used and the condition $\lambda = \sigma_n^2$ is met, the mean predictions of the GP Regressor closely follow the predictions of Kernel Ridge. To verify this, two cases are considered. In the first case, a GP Regressor using the Radial Basis Function (RBF) kernel with the length scale of 1 and $\sigma_n^2 = 1 \times 10^{-10}$, along with a Kernel Ridge using the same kernel with $\lambda = 1 \times 10^{-10}$, are trained. In this case, both models demonstrate strong alignment between observed data and their respective predictions. Additionally, both predictions closely match each other, as depicted in Figure A1. In the second case, illustrated in Figure A2, a GP Regressor using the DotProduct kernel with $\sigma_n^2 = 0$ (an equivalent representation of a linear kernel) is compared to a Kernel Ridge employing the linear kernel. Here, although there is a noticeable misalignment between observed data and predictions, the predictions of both models closely match each other, resembling the behavior observed in the first case. Moreover, in both scenarios, point-wise errors between predictions of GP Regressor and Kernel Ridge confirm these observations. Note that the kernel used in the first case is the kernel of the baseline GP Regressor, while the kernel used in the second case is the kernel of the baseline Kernel Ridge (see Figure 13). Therefore, we can see similar behavior on effects on the predictions.

References

- [1] D.J. Whitehouse, *Handbook of Surface Metrology* (Routledge & CRC Press, 1994). URL <https://www.routledge>.

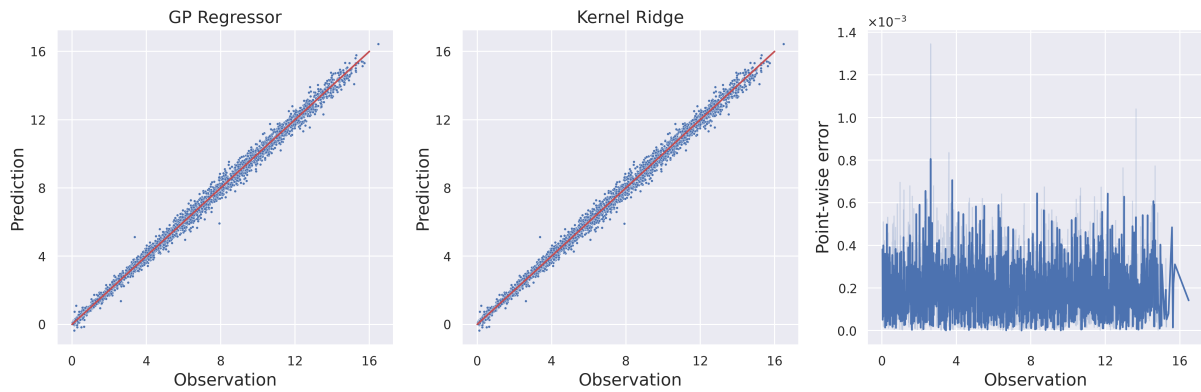


Fig. A1: Case 1: Good generalization.

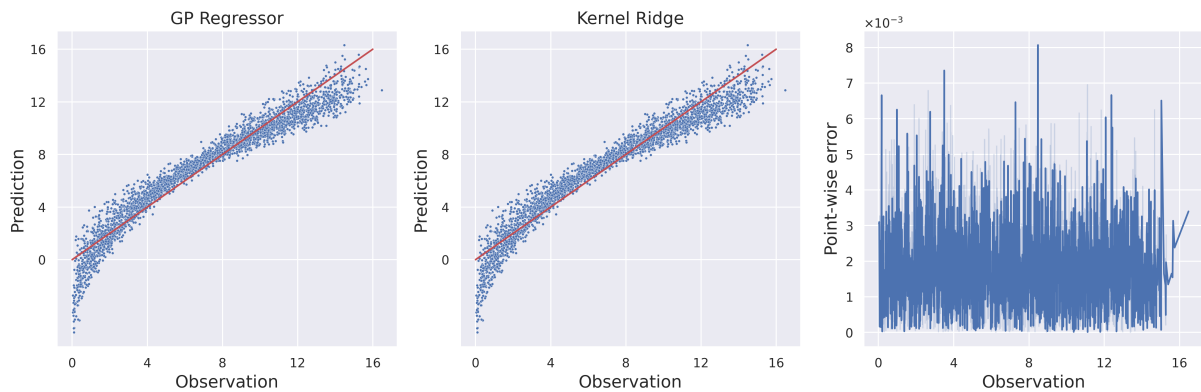


Fig. A2: Case 2: Bad generalization.

Fig. A3: Comparison of GP Regressor and Kernel Ridge under the assumption of both models having the same kernel including identical kernel parameters and the regularization parameter.

- com/Handbook-of-Surface-Metrology/Whitehouse/p/book/9780750300391
- [2] A. Vakis, V. Yastrebov, J. Scheibert, L. Nicola, D. Dini, C. Minfray, A. Almqvist, M. Paggi, S. Lee, G. Limbert, J. Molinari, G. Anciaux, R. Aghababaei, S. Echeverri Restrepo, A. Papangelo, A. Cammarata, P. Nicolini, C. Putignano, G. Carbone, S. Stupkiewicz, J. Lengiewicz, G. Costagliola, F. Bosia, R. Guarino, N. Pugno, M. Müser, M. Ciavarella, Modeling and simulation in tribology across scales: An overview. *Tribology International* **125**, 169–199 (2018). <https://doi.org/10.1016/j.triboint.2018.02.005>. URL <https://linkinghub.elsevier.com/retrieve/pii/S0301679X18300756>
- [3] J.A. Greenwood, J.B.P. Williamson, F.P. Bowden, Contact of nominally flat surfaces. *Proceedings of the Royal Society of London. Series A. Mathematical and Physical Sciences* **295**(1442), 300–319 (1966). <https://doi.org/10.1098/rspa.1966.0242>
- [4] J.R. Barber, M. Ciavarella, Contact mechanics. *International Journal of Solids and Structures* **37**(1), 29–43 (2000). [https://doi.org/https://doi.org/10.1016/S0020-7683\(99\)00075-X](https://doi.org/https://doi.org/10.1016/S0020-7683(99)00075-X). URL <https://www.sciencedirect.com/science/article/pii/S002076839900075X>
- [5] K.L. Johnson, *Contact Mechanics* (Cambridge University Press, 1985)

- [6] Y. Xu, R.L. Jackson, Boundary element method (BEM) applied to the rough surface contact vs. BEM in computational mechanics. *Friction* **7**(4), 359–371 (2019). <https://doi.org/10.1007/s40544-018-0229-3>. URL <http://link.springer.com/10.1007/s40544-018-0229-3>
- [7] P. Wriggers, G. Zavarise, Computational contact mechanics. *Computational Mechanics* **32**, 141 (2002). URL <https://api.semanticscholar.org/CorpusID:86572264>
- [8] A. Popp, M. Gitterle, M.W. Gee, W.A. Wall, A dual mortar approach for 3D finite deformation contact with consistent linearization. *International Journal for Numerical Methods in Engineering* **83**(11), 1428–1465 (2010). <https://doi.org/10.1002/nme.2866>. URL <http://dx.doi.org/10.1002/nme.2866>
- [9] P. Wriggers, *Advanced Discretization Methods for Contact Mechanics* (Springer International Publishing, Cham, 2018), pp. 87–123. https://doi.org/10.1007/978-3-319-90155-8_2. URL https://doi.org/10.1007/978-3-319-90155-8_2
- [10] M.F. Adams, Algebraic multigrid methods for constrained linear systems with applications to contact problems in solid mechanics. *Numerical Linear Algebra with Applications* **11**(2–3), 141–153 (2004). <https://doi.org/10.1002/nla.374>. URL <https://onlinelibrary.wiley.com/doi/10.1002/nla.374>
- [11] T.A. Wiesner, A. Popp, M.W. Gee, W.A. Wall, Algebraic multigrid methods for dual mortar finite element formulations in contact mechanics. *International Journal for Numerical Methods in Engineering* **114**(4), 399–430 (2018). <https://doi.org/10.1002/nme.5748>. URL <https://doi.org/10.1002/nme.5748>
- [12] T.A. Wiesner, M. Mayr, A. Popp, M.W. Gee, W.A. Wall, Algebraic multigrid methods for saddle point systems arising from mortar contact formulations. *International Journal for Numerical Methods in Engineering* **122**(15), 3749–3779 (2021). <https://doi.org/10.1002/nme.6680>. URL <https://doi.org/10.1002/nme.6680>
- [13] M. Mayr, A. Popp, Scalable computational kernels for mortar finite element methods. *Engineering with Computers* **39**(5), 3691–3720 (2023). <https://doi.org/10.1007/s00366-022-01779-3>. URL <https://doi.org/10.1007/s00366-022-01779-3>
- [14] R. Pohrt, Q. Li, Complete boundary element formulation for normal and tangential contact problems. *Physical Mesomechanics* **17**(4), 334–340 (2014). <https://doi.org/10.1134/S1029959914040109>. URL <https://doi.org/10.1134/S1029959914040109>
- [15] E.A.H. Vollebregt, A new solver for the elastic normal contact problem using conjugate gradients, deflation, and an FFT-based preconditioner. *Journal of Computational Physics* **257**, 333–351 (2014). <https://doi.org/10.1016/j.jcp.2013.10.005>. URL <https://www.sciencedirect.com/science/article/pii/S0021999113006724>
- [16] A. Bemporad, M. Paggi, Optimization algorithms for the solution of the frictionless normal contact between rough surfaces. *International Journal of Solids and Structures* **69–70**, 94–105 (2015). <https://doi.org/10.1016/j.ijsolstr.2015.06.005>. URL <https://linkinghub.elsevier.com/retrieve/pii/S0020768315002693>
- [17] M. Paggi, M. Ciavarella, The coefficient of proportionality k between real contact area and load, with new asperity models. *Wear* **268**(7–8), 1020–1029 (2010). <https://doi.org/10.1016/j.wear.2009.12.038>. URL <https://linkinghub.elsevier.com/retrieve/pii/S0043164809006607>
- [18] G. Carbone, F. Bottiglione, Asperity contact theories: Do they predict linearity between contact area and load? *Journal of the Mechanics and Physics of Solids* **56**(8), 2555–2572 (2008). <https://doi.org/10.1016/j.jmps.2008.03.011>. URL <https://linkinghub.elsevier.com/retrieve/pii/S0022509608000586>
- [19] V.A. Yastrebov, G. Anciaux, J.F. Molinari, The role of the roughness spectral

- breadth in elastic contact of rough surfaces. *Journal of the Mechanics and Physics of Solids* **107**, 469–493 (2017). <https://doi.org/10.1016/j.jmps.2017.07.016>. URL <https://linkinghub.elsevier.com/retrieve/pii/S0022509617303010>
- [20] C. Jacq, D. Nélias, G. Lormand, D. Girodin, Development of a three-dimensional semi-analytical elastic-plastic contact code. *Journal of Tribology* **124**(4), 653 – 667 (2002). <https://doi.org/10.1115/1.1467920>. URL <https://www.scopus.com/inward/record.uri?eid=2-s2.0-0036799432&doi=10.1115%2f1.1467920&partnerID=40&md5=956f3cae91a72df18c01f43f63a2f3e4>. Type: Article
- [21] C. Putignano, G. Carbone, A review of boundary elements methodologies for elastic and viscoelastic rough contact mechanics. *Physical Mesomechanics* **17**, 321–333 (2014). URL <https://api.semanticscholar.org/CorpusID:135893016>
- [22] J. Zhao, E.A. Vollebregt, C.W. Oosterlee, Extending the BEM for Elastic Contact Problems Beyond the Half-Space Approach. *Mathematical Modelling and Analysis* **21**(1), 119–141 (2016). <https://doi.org/10.3846/13926292.2016.1138418>. URL <https://doi.org/10.3846/13926292.2016.1138418>. Publisher: Taylor & Francis eprint: <https://doi.org/10.3846/13926292.2016.1138418>
- [23] S. Hyun, L. Pei, J.F. Molinari, M.O. Robbins, Finite-element analysis of contact between elastic self-affine surfaces. *Phys. Rev. E* **70**, 026117 (2004). <https://doi.org/10.1103/PhysRevE.70.026117>. URL <https://link.aps.org/doi/10.1103/PhysRevE.70.026117>
- [24] L. Pei, S. Hyun, J. Molinari, M. Robbins, Finite element modeling of elastoplastic contact between rough surfaces. *Journal of the Mechanics and Physics of Solids* **53**(11), 2385–2409 (2005). <https://doi.org/10.1016/j.jmps.2005.06.008>. URL <https://linkinghub.elsevier.com/retrieve/pii/S0022509605001225>
- [25] V.A. Yastrebov, J. Durand, H. Proudhon, G. Cailletaud, Rough surface contact analysis by means of the Finite Element Method and of a new reduced model. *Comptes Rendus. Mécanique* **339**(7-8), 473–490 (2011). <https://doi.org/10.1016/j.crme.2011.05.006>. URL <https://comptes-rendus.academie-sciences.fr/mecanique/articles/10.1016/j.crme.2011.05.006/>
- [26] R.P. Carvalho, A.M.C. Carneiro, F.M.A. Pires, A. Popp, An efficient algorithm for rigid/deformable contact interaction based on the dual mortar method. *Computational Mechanics* **71**(1), 143–167 (2023). <https://doi.org/10.1007/s00466-022-02226-2>. URL <https://link.springer.com/10.1007/s00466-022-02226-2>
- [27] M. Paggi, J. Reinoso, A variational approach with embedded roughness for adhesive contact problems. *Mechanics of Advanced Materials and Structures* **27**(20), 1731–1747 (2020). <https://doi.org/10.1080/15376494.2018.1525454>. URL <https://www.tandfonline.com/doi/full/10.1080/15376494.2018.1525454>
- [28] J. Bonari, M. Paggi, J. Reinoso, A framework for the analysis of fully coupled normal and tangential contact problems with complex interfaces. *Finite Elements in Analysis and Design* **196**, 103605 (2021). <https://doi.org/10.1016/j.finel.2021.103605>. URL <https://linkinghub.elsevier.com/retrieve/pii/S0168874X21000895>
- [29] J. Bonari, M. Paggi, D. Dini, A new finite element paradigm to solve contact problems with roughness. *International Journal of Solids and Structures* **253**, 111643 (2022). <https://doi.org/10.1016/j.ijsolstr.2022.111643>. URL <https://linkinghub.elsevier.com/retrieve/pii/S0020768322001640>
- [30] C. Campañá, M.H. Müser, Practical Green’s function approach to the simulation of elastic semi-infinite solids. *Physical Review B* **74**(7), 075420 (2006). <https://doi.org/10.1103/PhysRevB.74.075420>. URL <https://link.aps.org/doi/10.1103/PhysRevB.74.075420>

- [31] M.H. Müser, W.B. Dapp, R. Bugnicourt, P. Sainsot, N. Lesaffre, T.A. Lubrecht, B.N.J. Persson, K. Harris, A. Bennett, K. Schulze, S. Rohde, P. Ifju, W.G. Sawyer, T. Angelini, H. Ashtari Esfahani, M. Kadkhodaei, S. Akbarzadeh, J.J. Wu, G. Vorlaufer, A. Vernes, S. Solhjoo, A.I. Vakis, R.L. Jackson, Y. Xu, J. Streater, A. Rostami, D. Dini, S. Medina, G. Carbone, F. Bottiglione, L. Afferrante, J. Monti, L. Pastewka, M.O. Robbins, J.A. Greenwood, Meeting the Contact-Mechanics Challenge. *Tribology Letters* **65**(4), 118 (2017). <https://doi.org/10.1007/s11249-017-0900-2>. URL <http://link.springer.com/10.1007/s11249-017-0900-2>
- [32] J. Bonari, M.R. Marulli, N. Hagemeyer, M. Mayr, A. Popp, M. Paggi, A multi-scale FEM-BEM formulation for contact mechanics between rough surfaces. *Computational Mechanics* **65**(3), 731–749 (2020). <https://doi.org/10.1007/s00466-019-01791-3>. URL <http://link.springer.com/10.1007/s00466-019-01791-3>
- [33] D.P. Solomatine, A. Ostfeld, Data-driven modelling: some past experiences and new approaches. *Journal of Hydroinformatics* **10**(1), 3–22 (2008). <https://doi.org/10.2166/hydro.2008.015>. URL <https://doi.org/10.2166/hydro.2008.015>. <https://iwaponline.com/jh/article-pdf/10/1/3/386250/3.pdf>
- [34] F.J. Montáns, F. Chinesta, R. Gómez-Bombarelli, J.N. Kutz, Data-driven modeling and learning in science and engineering. *Comptes Rendus Mécanique* **347**(11), 845–855 (2019). <https://doi.org/https://doi.org/10.1016/j.crme.2019.11.009>. URL <https://www.sciencedirect.com/science/article/pii/S1631072119301809>. Data-Based Engineering Science and Technology
- [35] M. Bourdeau, X. qiang Zhai, E. Nefzaoui, X. Guo, P. Chatellier, Modeling and forecasting building energy consumption: A review of data-driven techniques. *Sustainable Cities and Society* **48**, 101533 (2019). <https://doi.org/https://doi.org/10.1016/j.scs.2019.101533>. URL <https://www.sciencedirect.com/science/article/pii/S2210670718323862>
- [36] K. Karapiperis, L. Stainier, M. Ortiz, J. Andrade, Data-driven multiscale modeling in mechanics. *Journal of the Mechanics and Physics of Solids* **147**, 104239 (2021). <https://doi.org/https://doi.org/10.1016/j.jmps.2020.104239>. URL <https://www.sciencedirect.com/science/article/pii/S0022509620304531>
- [37] R.D. Sanhueza, I. Akkerman, J.W. Peeters, Machine learning for the prediction of the local skin friction factors and nusselt numbers in turbulent flows past rough surfaces. *International Journal of Heat and Fluid Flow* **103**, 109204 (2023). <https://doi.org/https://doi.org/10.1016/j.ijheatfluidflow.2023.109204>. URL <https://www.sciencedirect.com/science/article/pii/S0142727X23001030>
- [38] M. Elangovan, N. Sakthivel, S. Saravanamurugan, B. Nair, V. Sugumaran, Machine learning approach to the prediction of surface roughness using statistical features of vibration signal acquired in turning. *Procedia Computer Science* **50**, 282–288 (2015). <https://doi.org/https://doi.org/10.1016/j.procs.2015.04.047>. URL <https://www.sciencedirect.com/science/article/pii/S1877050915005487>. Big Data, Cloud and Computing Challenges
- [39] D.K. Prajapati, J.K. Katiyar, C. Prakash, Machine learning approach for the prediction of mixed lubrication parameters for different surface topographies of non-conformal rough contacts. *Industrial Lubrication and Tribology* **75**(9), 1022–1030 (2023). <https://doi.org/https://doi.org/10.1108/ILT-04-2023-0121>
- [40] G. Boidi, M.R. da Silva, F.J. Profito, I.F. Machado, Using machine learning radial basis function (rbf) method for predicting lubricated friction on textured and porous surfaces. *Surface Topography: Metrology and Properties* **8**(4), 044002 (2020). <https://doi.org/10.1088/2051-672X/abae13>. URL <https://dx.doi.org/10.1088/2051-672X/abae13>

- [41] M.S. Hasan, M. Nosonovsky, Triboinformatics: machine learning algorithms and data topology methods for tribology. *Surface Innovations* **10**(4-5), 229–242 (2022). <https://doi.org/10.1680/jsuin.22.00027>. URL <https://doi.org/10.1680/jsuin.22.00027>. <https://doi.org/10.1680/jsuin.22.00027>
- [42] T. Batu, H.G. Lemu, H. Shimels, Application of artificial intelligence for surface roughness prediction of additively manufactured components. *Materials (Basel)* **16**(18) (2023)
- [43] M. Rapetto, A. Almqvist, R. Larsson, P. Lugt, On the influence of surface roughness on real area of contact in normal, dry, friction free, rough contact by using a neural network. *Wear* **266**(5-6), 592–595 (2009)
- [44] K. Kalliorinne, R. Larsson, F. Pérez-Ràfols, M. Liwicki, A. Almqvist, Artificial neural network architecture for prediction of contact mechanical response. *Frontiers in Mechanical Engineering* **6**, 579825 (2021). <https://doi.org/10.3389/fmech.2020.579825>
- [45] J. Jiang, W. Zhang, D. Guo, L. Yu, Prediction of real contact area of fractal rough surface based on fem contact model results and support vector machine algorithm. *Journal of Computational Methods in Sciences and Engineering* **21**(1), 223–231 (2021). <https://doi.org/10.3233/JCM-204491>
- [46] M. Raissi, P. Perdikaris, G. Karniadakis, Physics-informed neural networks: A deep learning framework for solving forward and inverse problems involving nonlinear partial differential equations. *Journal of Computational Physics* **378**, 686–707 (2019). <https://doi.org/https://doi.org/10.1016/j.jcp.2018.10.045>
- [47] T. Sahin, M. Von Danwitz, A. Popp, Solving forward and inverse problems of contact mechanics using physics-informed neural networks. *Advanced Modeling and Simulation in Engineering Sciences* **11**(1), 11 (2024). <https://doi.org/10.1186/s40323-024-00265-3>
- [48] K.L. Johnson, *Contact Mechanics* (Cambridge University Press, 1985). <https://doi.org/10.1017/CBO9781139171731>
- [49] F.P. Bowden, D. Tabor, *Friction and Lubrication of Solids* (Oxford: Clarendon Press, 1950)
- [50] A. Vakis, V. Yastrebov, J. Scheibert, L. Nicola, D. Dini, C. Minfray, A. Almqvist, M. Paggi, S. Lee, G. Limbert, J. Molinari, G. Anciaux, R. Aghababaei, S. Echeverri Restrepo, A. Papangelo, A. Cammarata, P. Nicolini, C. Putignano, G. Carbone, S. Stupkiewicz, J. Lengiewicz, G. Costagliola, F. Bosia, R. Guarino, N. Pugno, M. Müser, M. Ciavarella, Modeling and simulation in tribology across scales: An overview. *Tribology International* **125**, 169–199 (2018). <https://doi.org/https://doi.org/10.1016/j.triboint.2018.02.005>
- [51] J. Barber, *Contact Mechanics* (Springer, 2018)
- [52] V.A. Yastrebov, G. Anciaux, J.F. Molinari, From infinitesimal to full contact between rough surfaces: Evolution of the contact area. *International Journal of Solids and Structures* **52**, 83–102 (2015). <https://doi.org/https://doi.org/10.1016/j.ijsolstr.2014.09.019>. URL <https://www.sciencedirect.com/science/article/pii/S0020768314003667>
- [53] A. Fournier, D. Fussell, L. Carpenter, Computer rendering of stochastic models. *Commun. ACM* **25**(6), 371–384 (1982). <https://doi.org/10.1145/358523.358553>
- [54] B.N.J. Persson, On the fractal dimension of rough surfaces. *Tribology Letters* **54**(1), 99–106 (2014). <https://doi.org/10.1007/s11249-014-0313-4>
- [55] B. Mandelbrot, *The fractal geometry of nature* (San Francisco: W.H. Freeman, 1984)
- [56] M.F. Barnsley, R.L. Devaney, B.B. Mandelbrot, H.O. Peitgen, D. Saupe, R.F. Voss, Y. Fisher, M. McGuire, *The science of fractal images*, vol. 1 (Springer, 1988)

- [57] A. Bemporad, M. Paggi, Optimization algorithms for the solution of the frictionless normal contact between rough surfaces. *International Journal of Solids and Structures* **69-70**, 94–105 (2015). <https://doi.org/https://doi.org/10.1016/j.ijsolstr.2015.06.005>
- [58] G. Zavarise, M. Borri-Brunetto, M. Paggi, On the reliability of microscopical contact models. *Wear* **257**(3), 229–245 (2004). <https://doi.org/https://doi.org/10.1016/j.wear.2003.12.010>
- [59] M. Paggi, M. Ciavarella, The coefficient of proportionality κ between real contact area and load, with new asperity models. *Wear* **268**(7), 1020–1029 (2010). <https://doi.org/https://doi.org/10.1016/j.wear.2009.12.038>
- [60] C. Borri, M. Paggi, Topological characterization of antireflective and hydrophobic rough surfaces: are random process theory and fractal modeling applicable? *Journal of Physics D: Applied Physics* **48**(4), 045301 (2015). <https://doi.org/10.1088/0022-3727/48/4/045301>
- [61] L. Frérot, G. Anciaux, V. Rey, S. Pham-Ba, J.F. Molinari, Tamaas: a library for elastic-plastic contact of periodic rough surfaces. *Journal of Open Source Software* **5**(51), 2121 (2020). <https://doi.org/10.21105/joss.02121>. URL <https://doi.org/10.21105/joss.02121>
- [62] J.D. Bordón, G.M. Álamo, L.A. Padrón, J.J. Aznárez, O. Maeso, Multifebe: A multi-domain finite element–boundary element solver for linear mixed-dimensional mechanical problems. *SoftwareX* **20**, 101265 (2022). <https://doi.org/https://doi.org/10.1016/j.softx.2022.101265>
- [63] V.L. Popov, M. Heß, E. Willert, *Handbook of contact mechanics: exact solutions of axisymmetric contact problems* (Springer Nature, 2019)
- [64] S. Brandstaeter, S.L. Fuchs, J. Biehler, R.C. Aydin, W.A. Wall, C.J. Cyron, Global Sensitivity Analysis of a Homogenized Constrained Mixture Model of Arterial Growth and Remodeling. *Journal of Elasticity* **145**(1-2), 191–221 (2021). <https://doi.org/10.1007/s10659-021-09833-9>
- [65] B. Wirthl, S. Brandstaeter, J. Nitzler, B.A. Schrefler, W.A. Wall, Global sensitivity analysis based on Gaussian-process metamodelling for complex biomechanical problems. *International Journal for Numerical Methods in Biomedical Engineering* **39**(3), e3675 (2023). <https://doi.org/10.1002/cnm.3675>
- [66] H. Willmann, J. Nitzler, S. Brandstätter, W.A. Wall, Bayesian calibration of coupled computational mechanics models under uncertainty based on interface deformation **9**(1), 24. <https://doi.org/10.1186/s40323-022-00237-5>. URL <https://doi.org/10.1186/s40323-022-00237-5>
- [67] M. Dinkel, C.M. Geitner, G. Robalo Rei, J. Nitzler, W.A. Wall, Solving Bayesian inverse problems with expensive likelihoods using constrained Gaussian processes and active learning. *Inverse Problems* **40**(9), 095008 (2024). <https://doi.org/10.1088/1361-6420/ad5eb4>
- [68] M. von Danwitz, T.T. Kochmann, T. Sahin, J. Wimmer, T. Braml, A. Popp, Hybrid digital twins: A proof of concept for reinforced concrete beams. *Proceedings in Applied Mathematics and Mechanics* **22**(1), e202200146 (2023)
- [69] T. Sahin, D. Wolff, M. von Danwitz, A. Popp, Towards a hybrid digital twin: Fusing sensor information and physics in surrogate modeling of a reinforced concrete beam pp. 1–8 (2024). <https://doi.org/10.1109/SDF63218.2024.10773885>
- [70] H. Ganti, P. Khare, Data-driven surrogate modeling of multiphase flows using machine learning techniques. *Computers & Fluids* **211**, 104626 (2020). <https://doi.org/https://doi.org/10.1016/j.compfluid.2020.104626>
- [71] R. Goodman, L. Kish, Controlled selection—a technique in probability sampling. *Journal of the American Statistical Association* **45**(251), 350–372 (1950)

- [72] A. Géron, *Hands-on machine learning with Scikit-Learn, Keras, and TensorFlow* (O'Reilly Media, Inc., 2022)
- [73] D. Singh, B. Singh, Investigating the impact of data normalization on classification performance. *Applied Soft Computing* **97**, 105524 (2020). <https://doi.org/https://doi.org/10.1016/j.asoc.2019.105524>
- [74] X. Wu, V. Kumar, J. Ross Quinlan, J. Ghosh, Q. Yang, H. Motoda, G.J. McLachlan, A. Ng, B. Liu, P.S. Yu, Z.H. Zhou, M. Steinbach, D.J. Hand, D. Steinberg, Top 10 algorithms in data mining. *Knowledge and Information Systems* **14**(1), 1–37 (2008). <https://doi.org/10.1007/s10115-007-0114-2>
- [75] L. Breiman, Random forests. *Machine Learning* **45**(1), 5–32 (2001). <https://doi.org/10.1023/A:1010933404324>
- [76] V.N. Vapnik, *The nature of statistical learning theory* (Springer-Verlag New York, Inc., 1995)
- [77] Y. Freund, R.E. Schapire, A decision-theoretic generalization of on-line learning and an application to boosting. *Journal of Computer and System Sciences* **55**(1), 119–139 (1997). <https://doi.org/https://doi.org/10.1006/jcss.1997.1504>
- [78] C.E. Rasmussen, C.K.I. Williams, *Gaussian Processes for Machine Learning* (The MIT Press, 2005). <https://doi.org/10.7551/mitpress/3206.001.0001>
- [79] J.H. Friedman, Greedy function approximation: A gradient boosting machine. *The Annals of Statistics* **29**(5), 1189 – 1232 (2001). <https://doi.org/10.1214/aos/1013203451>
- [80] V. Vovk, *Kernel Ridge Regression* (Springer Berlin Heidelberg, Berlin, Heidelberg, 2013), pp. 105–116. https://doi.org/10.1007/978-3-642-41136-6_11
- [81] T. Chen, C. Guestrin, Xgboost: A scalable tree boosting system p. 785–794 (2016). <https://doi.org/10.1145/2939672.2939785>
- [82] I. Goodfellow, Y. Bengio, A. Courville, *Deep Learning* (MIT Press, 2016). <http://www.deeplearningbook.org>
- [83] K.P. Murphy, *Machine Learning: A Probabilistic Perspective* (The MIT Press, 2012)
- [84] L. Yang, A. Shami, On hyperparameter optimization of machine learning algorithms: Theory and practice. *Neurocomputing* **415**, 295–316 (2020). <https://doi.org/https://doi.org/10.1016/j.neucom.2020.07.061>
- [85] M. Feurer, F. Hutter, *Hyperparameter Optimization* (Springer International Publishing, Cham, 2019), pp. 3–33. https://doi.org/10.1007/978-3-030-05318-5_1
- [86] Y. Gorishniy, I. Rubachev, V. Khrulkov, A. Babenko, Revisiting deep learning models for tabular data. *arXiv* **2106.11959** (2021)
- [87] F. Pedregosa, G. Varoquaux, A. Gramfort, V. Michel, B. Thirion, O. Grisel, M. Blondel, P. Prettenhofer, R. Weiss, V. Dubourg, J. Vanderplas, A. Passos, D. Cournapeau, M. Brucher, M. Perrot, E. Duchesnay, Scikit-learn: Machine learning in Python. *Journal of Machine Learning Research* **12**, 2825–2830 (2011)
- [88] R. Kohavi, A study of cross-validation and bootstrap for accuracy estimation and model selection p. 1137–1143 (1995)
- [89] X. Zhang, C.A. Liu, Model averaging prediction by k-fold cross-validation. *Journal of Econometrics* **235**(1), 280–301 (2023). <https://doi.org/https://doi.org/10.1016/j.jeconom.2022.04.007>
- [90] A. Botchkarev, A new typology design of performance metrics to measure errors in machine learning regression algorithms. *Interdisciplinary Journal of Information, Knowledge, and Management* **14**, 45 – 79 (2019). <https://doi.org/https://doi.org/10.28945/4184>
- [91] R.J. Hyndman, A.B. Koehler, Another look at measures of forecast accuracy. *International Journal of Forecasting* **22**(4), 679–688

(2006). <https://doi.org/https://doi.org/10.1016/j.ijforecast.2006.03.001>